FAILURE AND CRIPPLING OF GRAPHITE-EPOXY STIFFENERS LOADED IN COMPRESSION

by

Stephen T. Tyahla

Thesis submitted to the Faculty of the

Virginia Polytechnic Institute and State University

in partial fulfillment of the requirements for the degree of

MASTER OF SCIENCE

in

Aerospace and Ocean Engineering

APPROVED:

Eric R. Johnson

William L. Hallauer, Jr.

Carl T. Herakovich

May, 1984
Blacksburg, Virginia

FAILURE AND CRIPPLING OF GRAPHITE-EPOXY STIFFENERS LOADED IN COMPRESSION

by

Stephen T. Tyahla

(ABSTRACT)

Results of an experimental study of the failure and crippling of thin-walled open section prismatic compression members are presented. Twenty-four specimens were tested, 13 of which were channel sections and the other 11 were zee sections. Three specimens were made of 2024-T3 aluminum. The remaining 21 specimens were made of AS4-3502 graphite-epoxy. All specimens were tested to failure.

Seventeen specimens exhibited local buckling of flanges and webs prior to failure, four exhibited global column buckling prior to failure, two exhibited material short column failure, and one exhibited unstable postbuckling behavior prior to failure. The buckling loads for each specimen were also calculated by a computer code and compared to experimental buckling loads. Good correlation was achieved for specimens that did not buckle as columns.

The graphite-epoxy specimens which buckled locally had significant postbuckling response prior to failure at a maximum load (crippling). Differences in the crippling failure and compressive strength failure are discussed for the graphite-epoxy specimens.

ACKNOWLEDGEMENTS

This project was supported by the NASA-Virginia Tech Composites Program through NASA Grant NAG1-343. I am grateful to Dr. James H. Starnes Jr. and the Structural Mechanics Branch of NASA Langley Research Center for the assistance and use of the facilities I needed during this project.

I am greatly indebted to Dr. Eric Johnson for his patient supervision during this project. His timely suggestions were greatly appreciated.

I also thank Dr. William Hallauer Jr. and Dr. Carl Herakovich for serving on my committee.

I would like to thank Dr. W. B. Gross for his rapid "last-minute" photographic work.

Finally I would like to thank my very dear friend Linda Gross for her constant support and understanding during this project.

TABLE OF CONTENTS

Appendix

page

LIST OF TABLES

LIST OF FIGURES

Chapter I

INTRODUCTION

Aerospace structures are designed for maximum efficiency. They must carry the required loads and weigh as little as possible. A design which minimizes the weight of these structures consists of thin skins supported by stiffening members. The skins of these structures are designed to carry shear loads and the stiffeners support the skin by carrying tensile or compressive loads. The compressive loading can lead to a phenomenon known as stiffener crippling, which is a major topic in this report.

1.1 DEFINITION OF STIFFENER CRIPPLING

In order to be effective, stiffeners must be fastened to skins securely. The most common method of fastening metal stiffeners to skins involves the use of mechanical fasteners, such as rivets, which are closely spaced to provide the skin with good support from the stiffener. Methods for fastening composite stiffeners to skins include stitching, bonding, or use of mechanical fasteners to provide closely spaced support. In any case, the important point is that for skin-stiffener structures to be effective, the fastening method must involve closely spaced or continuous connection

between skin and stiffener so that the skin is supported by the stiffener as completely as possible.

Stiffener sections consist of plate elements joined together in configurations that provide bending stiffness for the structure. When loaded in axial compression, a free standing stiffener can either buckle locally, exhibiting short wavelength plate behavior, or buckle globally, exhibiting long wavelength column behavior. The type of behavior depends on the geometry of the stiffener. If a stiffener is fastened to the skin, as previously discussed, and it is loaded in compression, it will buckle locally with short wavelength plate behavior because of the closely spaced restraint of the fastening method. Upon further loading, the stiffener will exhibit postbuckling strength supplied by its plate elements and finally fail at a maximum load level. This failure in the postbuckling range following local buckling is commonly referred to as local crippling. In this report the local crippling of stiffeners will be referred to as stiffener crippling.

1.2 REVIEW OF METAL STIFFENER CRIPPLING WORK

Original efforts to understand the phenomenon of stiffener crippling were made before composite materials were developed. Much of the literature, therefore, concerns analysis performed on isotropic metal stiffener sections.

The work done in metal stiffener crippling was motivated by knowledge of the fact that the strength of a stiffener was related to its critical (buckling) stress [1] . In order to understand how a stiffener failed it was necessary to first understand how it buckled. Channel and zee sections have critical elements. For either section, the flanges or the web can drive the buckling process. As the stiffener is loaded, the critical element requires restraint from adjacent elements to delay buckling. When the critical load is reached, the entire section buckles as a whole. During buckling, the joints (corners) between plate elements remain in their original straight lines but rotate. The rotation is controlled by the same elastic restraint from interconnected elements that previously delayed buckling [1].

In principle, the determination of the stiffness of an element's elastic restraint requires the application of a moment along the edge of the element, the measurement of the rotation along the edge of the element, and the calculation

of the ratio between the moment and rotation. This ratio is the rotational stiffness of the element, and it is a function of the compressive stress applied to the element.

The condition for neutral stability of a cross section composed of plate elements is that the sum of the stiffnesses of all the elements entering a common joint is zero. This condition is commonly called the joint-stiffness criterion [2]. In order to determine the buckling load of a stiffener section, the joint-stiffness criterion is applied as follows. A series of values of buckling stresses is assumed, and for each stress the stiffnesses of the elements meeting at a joint are calculated. The lowest stress for which the stiffnesses add to zero is the buckling stress.

Prior to buckling, the stress distribution across the loaded edge of a plate is uniform. After buckling, the central warped region of the plate carries less load as more load is redistributed into the stiff straight unloaded edges. Failure occurs when the edges cannot carry the increasing loads because the edge stresses exceed the yield stress.

Von Kármán [2] approximated this behavior as follows. He proposed that failure of plates (as opposed to built-up sections) was related to the yield stress of the material. Von Kármán's model supposes that two longitudinal edge strips,

each of width (m/2)*b, (0<m<1), carry the entire postbuckling compressive load applied to a plate of width b. The width m*b is known as the effective width of the plate. The central section, of width (1-m)*b, supports no load. The failure load then, is reached when the uniform stress in the edge strips equals the yield stress of the material.

From the previous discussion, it is apparent that after elastic buckling the failure stress and the yield stress of the material are related. Theory and tests [3] indicate that the following relation between the average applied stress σ, and the edge stress σ_e is a good approximation of postbuckling behavior.

$$\frac{\bar{\sigma}}{\sigma_{cr}} = \alpha\left(\frac{\sigma_e}{\sigma_{cr}}\right)^n \tag{1}$$

If it is assumed that failure occurs when the edge stress equals the yield stress, equation (1) becomes

$$\frac{\sigma_f}{\sigma_{cr}} = \alpha\left(\frac{\sigma_{cy}}{\sigma_{cr}}\right)^n \tag{2}$$

where σ_f is the crippling stress, σ_{cr} is the buckling stress and σ_{cy} is the compressive yield stress [3]. The formulation is empirical in nature and has been used to present

data for stiffener sections composed of plate elements. Schuette [4] plotted data for zee and channel sections and showed that for a specific value b_w/t, (web width to wall thickness ratio) the parameters α and n were constant. When a log-log plot of $\frac{\sigma_f}{\sigma_{cr}}$ vs. $\frac{\sigma_{cy}}{\sigma_{cr}}$ is made, the data fall on a straight line. The parameter α is the intercept, (i.e. the value of $\frac{\sigma_f}{\sigma_{cr}}$ at $\frac{\sigma_{cy}}{\sigma_{cr}}$ =1) and the parameter n is the slope of the line.

The previous discussion pertains to metal stiffener crippling after elastic buckling. Methods for determining the crippling strength of stiffeners after plastic buckling have also been used. In Peery [5] a formulation for stiffener crippling strength is presented that involves a summation of plastic buckling loads of the n plate elements of the stiffener. The formulation is

$$F_{cc} = \frac{F_1 b_1 t_1 + F_2 b_2 t_2 + \cdots + F_n b_n t_n}{b_1 t_1 + b_2 t_2 + \cdots + b_n t_n} \quad . \tag{3}$$

In this formula the buckling load F_n is defined by the equation

$$F_n = K\, E_t \left(\frac{t_n}{b_n}\right)^2 \quad . \tag{4}$$

This equation is the same as the one used for elastic buckling prediction, except that the tangent modulus E_t has been

substituted for the elastic modulus E. The buckling parameter K, which depends on the aspect ratio, the plate thickness, t, and the plate width (excluding corner sections), b, are the same parameters used in the elastic formulation.

1.3 REVIEW OF COMPOSITE STIFFENER CRIPPLING WORK

Most of the work done on crippling of composite plates and stiffener sections has been done by Spier [e.g. 6 and 7] In his work, Spier uses a variation of the empirical metals formulation, equation (2), to present his composite data. Spier's formulation for plates is

$$\frac{F^{CC}}{F^{CR}} = \alpha \left(\frac{F^{CU}}{F^{CR}} \right)^{n} \qquad (5)$$

In this formulation, F^{CC} is the crippling stress, F^{CR} is the buckling stress, and F^{CU} is the ultimate compressive strength of the laminate [6]. The obvious difference between Spier's formulation and that used by Schuette for metals is the appearance of F^{CU} (compressive strength) instead of σ_{cy} (yield stress). Instead of relating crippling to buckling and yielding as was done with metals, Spier relates crippling to buckling and compressive strength. Spier suggests that F^{CU} values can be obtained by testing plates with small b/t ratios (around 6) [7]. In

this configuration, the plate will fail in compression rather than in buckling.

For built-up stiffener sections, Spier uses a variation of a formulation used by Gallaher and Needham [8] to present metals data. The formulation used for metals is

$$\sigma_f = C\left(\frac{t^2}{A}\right)^m \quad , \tag{6}$$

where σ_f is the crippling stress, t is the wall thickness and A is the cross-sectional area of the stiffener. C and m are constants . Spier's formulation is

$$\frac{F^{CC}}{F^{CU}} = \beta \left(\frac{t^2}{A}\sqrt{\frac{E^*}{F^{CU}}}\right)^m \quad , \tag{7}$$

where

$$E^* = \frac{12}{t^3}\sqrt{D_{11}D_{22}} \quad , \tag{8}$$

in which D_{11}, and D_{22} are laminate bending stiffnesses, β and m are constants, and all other parameters have previously been defined [9].

For built-up sections, Spier has not interrelated the crippling stress F^{CC}, the buckling stress F^{CR} , and the ultimate compressive strength F^{CU}, as he does in the plate formulation (5). Instead, he has separate non-dimensional

formulas for crippling (equation 7) and buckling. The non-dimensional buckling formula is

$$\frac{F_{CH}^{CR}}{F^{CU}} = K_{CH}^{CR} \left(\frac{t^2}{A} \sqrt{\frac{E^*}{F^{CU}}} \right)^2 , \qquad (9)$$

where F_{CH}^{CR} is the channel buckling stress and K_{CH}^{CR} is the channel buckling constant [9]. The buckling constant used in the formula is the smaller of two values. One value corresponds to no-edge-free buckling (i.e. the web buckles first). The other value corresponds to one-edge-free buckling (i.e. the flange buckles first). Spier's buckling formula then, predicts buckling of a built-up section by predicting which element (web or flange) of the section will buckle first, independently of the element attached to it. For metallic stiffeners, element stiffness interaction was taken into account when calculating the section buckling load.

1.4 OBJECTIVES OF THE PRESENT STUDY

It is apparent that little work has been done on the postbuckling failures of graphite-epoxy composite stiffeners that are thin walled open sections. The objective of this study is to investigate the experimental response and failure of thin walled open section stiffeners made from gra-

phite-epoxy subject to axial compression. This project will lay the ground work for later investigations of local crippling of graphite-epoxy stiffeners. It will supply the preliminary experimentation that is needed before theoretical models can be developed and extensive numerical analyses can be attempted.

In addition to the local crippling mode of failure, some other modes of failure occured in this study. For example, some of the stiffener geometries buckled as columns. This category includes channel sections that buckle in combined torsional/strong-axis modes and zee sections that buckle by bending about their weak axis. The failure of stiffener sections that exhibited very little postbuckling behavior and failed in essentially pure compression also occured. This category includes one channel and one zee specimen. The last category includes one zee specimen that is an interesting anomaly. It exhibited unstable postbuckling behavior prior to failure.

Chapter II

TESTING

2.1 DESCRIPTION OF SPECIMENS

The specimens used in this study were made of AS4-3502 graphite-epoxy unidirectional tape. This material system is a product of Hercules Incorporated. The fabrication was performed by Lockheed Georgia Company. In addition to the graphite-epoxy specimens, specimens made of 2024-T3 aluminum were fabricated. The metal specimens were included so that comparisons could be made between metal and graphite-epoxy tests.

All specimens were either channel or zee stiffeners (see Figure 1). In both configurations, the cross section consisted of a central web and two equal-width flanges. The web width, b_w, for all specimens was 1.25 inches. The flange widths, b_f, for the specimens were either 0.75 inches or 1.25 inches. The aluminum specimens were formed and the graphite-epoxy specimens were autoclave cured. In either case, each specimen had equal corner radii, R, at both web-flange junctions. The inner corner radii for each specimen were either 0.125 inches or 0.250 inches. The web and flanges of each specimen were of equal thickness. The nominal wall thickness, t_w, for a specimen was either 0.040 inches or 0.080 inches.

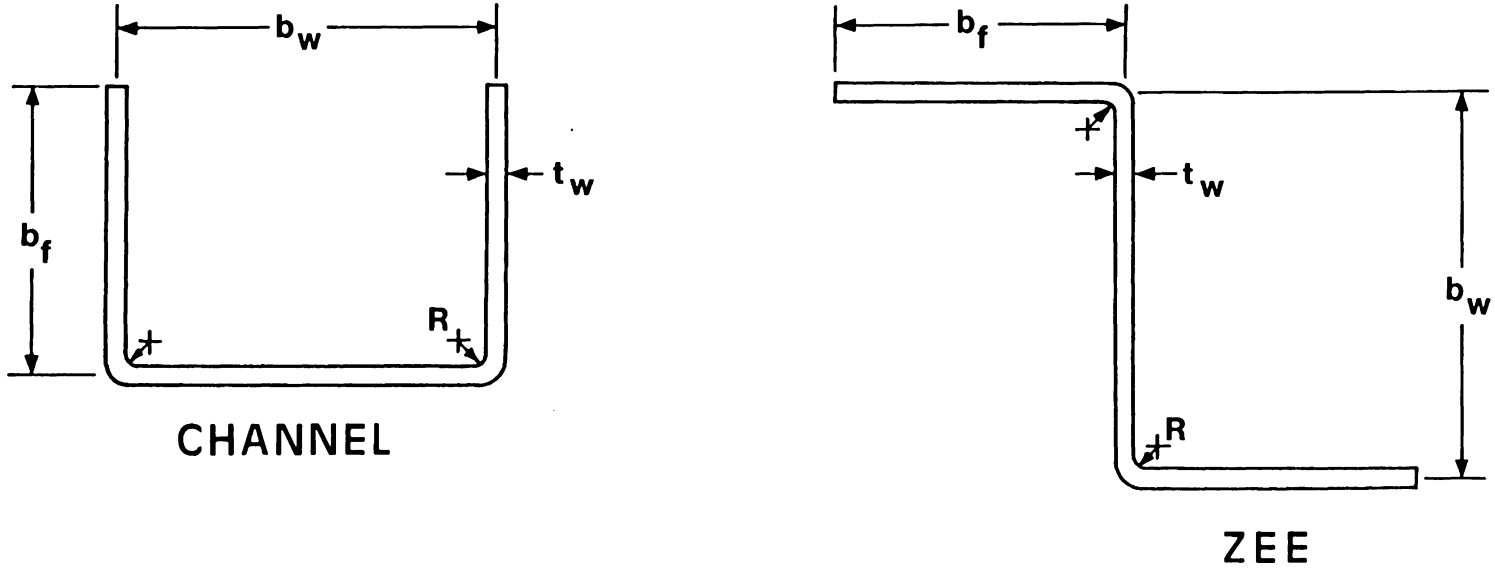

$b_w \equiv$ web width

$b_f \equiv$ flange width

$R \equiv$ inner corner radius

$t_w \equiv$ wall thickness

Figure 1: Channel and Zee Cross-Sectional Geometries

The graphite-epoxy specimens were fabricated from AS4-3502 tape. When cured, the material had a nominal ply thickness of 0.005 inches. To achieve a wall thickness of 0.040 inches or 0.080 inches, the specimens were made of 8-ply or 16-ply laminates respectively.

The stacking sequence for the 8-ply laminates was $[\pm 45/0/90]_S$. This sequence produced quasi-isotropic properties. For the 16-ply laminates, there were two stacking sequences. The first sequence, which is referred to as 16A, was $[\pm 45/0/90]_{2S}$ doubled the 8-ply sequence and also produced quasi-isotropic properties. The second sequence, which is referred to as 16B, was $[\pm 45/\mp 45/90/0_3]_S$ and produced orthotropic properties.

This study involved compression testing of specimens. Therefore, the ends of the specimens were prepared for a compressive loading condition. During tensile testing, a secure grip on the specimen is required for uniform loading. During compressive testing, a flat wide area on the end of the specimen is desirable for uniform load introduction. In addition to providing for uniform load introduction, the flat wide area provides much needed stability and friction at the end of the specimen to prevent slipping along the loading head. The flat wide area was produced by potting all specimens tested in this project.

Each end of each specimen was set in potting compound in a supporting structure such as a metal ring or wooden block to prevent end brooming failures. (see Figure 2). After the potting compound solidified, the specimen ends, the potting compound, and the supporting structure were ground flat and parallel to insure uniform and stable load introduction.

With the geometric parameters defined, an explanation of the specimen identification code used in this study can now be presented. The convention described each specimen in terms of its cross-sectional geometry, stacking sequence, and exposed length between the potted ends. Each specimen was given a code name in the form,

SHAPE	-	FLANGE WIDTH	-	INNER CORNER RADIUS	-	STACKING SEQUENCE	-	EXPOSED LENGTH

For example a channel section with a flange width of 1.25 inches, an inner corner radius of 1/8 inch, a stacking sequence of 16A, and exposed length of 12 inches was designated as,

C - 1.25 - 1/8 - 16A - 12.0

For a zee specimen, the C in the designation would be replaced by a Z. For an aluminum section, the stacking sequence would be replaced by the wall thickness in inches. An aluminum zee with a wall thickness of .040 inches with the same geometry as the channel above would be,

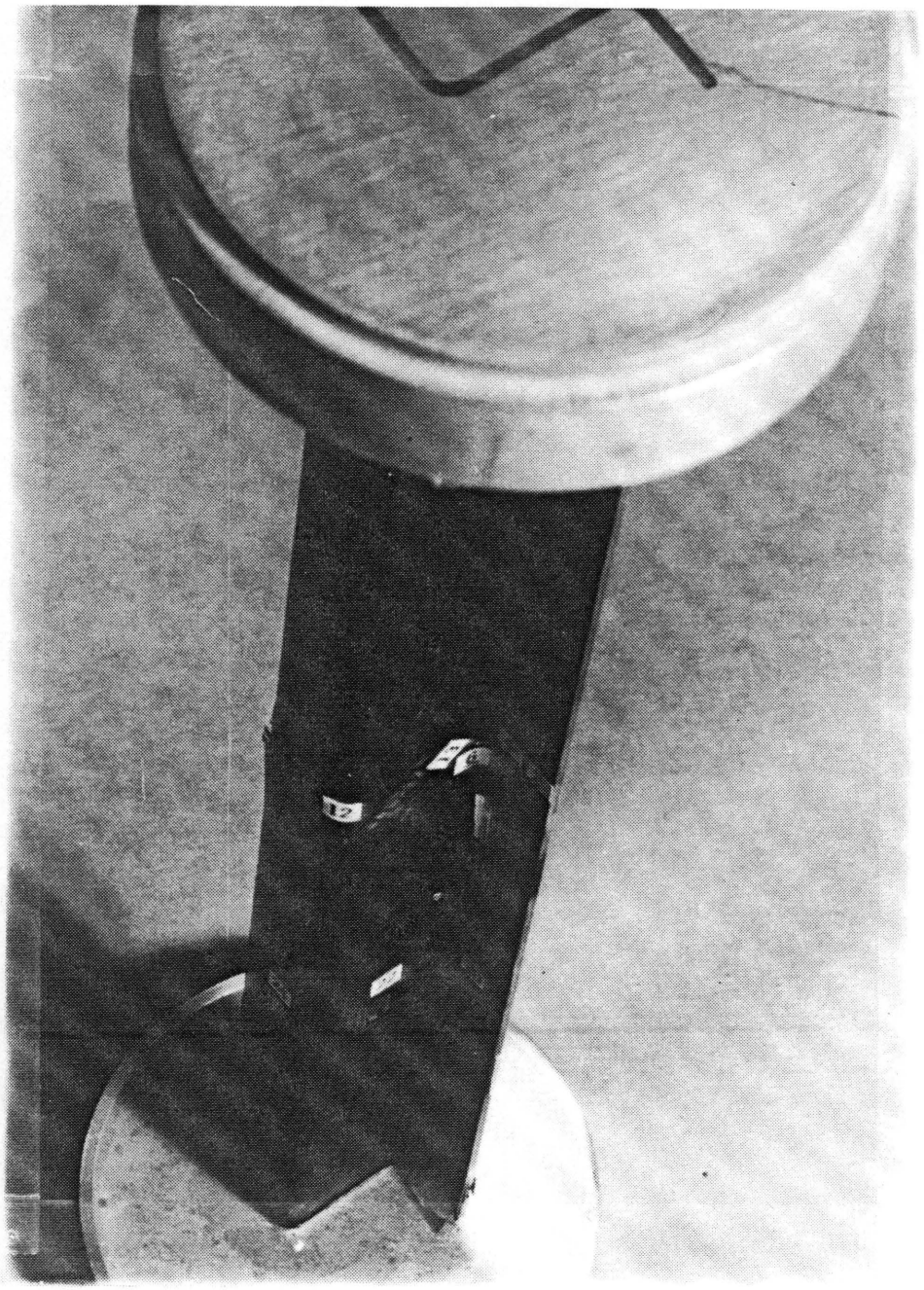

Figure 2: Specimen Potted at Both Ends

Z - 1.25 - 1/8 - .04 - 12.0

The only dimension of the specimen not yet discussed is the length. The length was treated as a design variable that controlled the behavior of the specimen. A short specimen will buckle locally and a long one will buckle as a column. The computer code PASCO [10] was used to determine the length of the specimens. PASCO is a design code for sizing minimum-weight stiffened panels subject to buckling constraints. PASCO incorporates VIPASA [11] for the buckling analysis of structures consisting of a prismatic assembly of plate elements.

The basis for VIPASA is to assume a buckling mode for each plate element in the assembly which is sinusoidal along the length with a half wavelength λ. The intersection of the plate elements in the assembly are assumed to be rigid joints. Using the cross-sectional dimensions and laminate lay-ups for the channel and zee section stiffeners in this study, a plot of the buckling load versus λ was generated for each specimen. Figure 3 shows a typical plot of buckling load versus λ. From the load versus half wavelength relationship, a length referred to as the transition length, L_T , was determined. The transition length is the length at which the buckling behavior of the stiffener shifts from

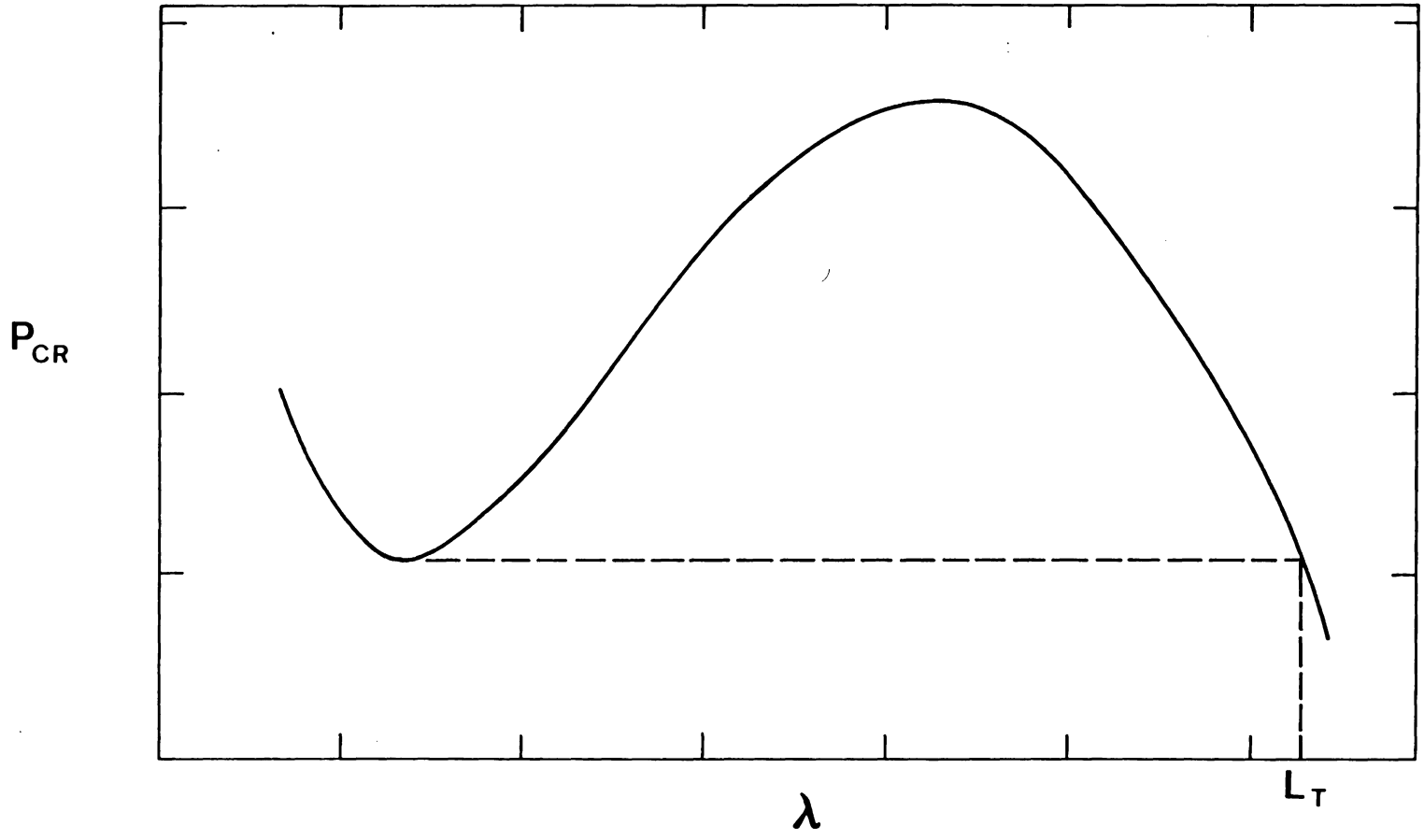

Figure 3: Determination of Transition Length

short wavelength local plate buckling to long wavelength global column buckling (see Figure 4). Cutting the specimen shorter than the transition length caused the specimen to exhibit local plate buckling. Cutting the specimen longer than the transition length caused the specimen to exhibit global column buckling.

The VIPASA solutions were restricted to problems with simple support boundary conditions at the loaded ends. Potting the ends of the specimens, makes the experimental boundary conditions closer to clamped than simply supported. This difference in end conditions was not significant in local plate buckling cases but it was very significant in global buckling cases. For local plate buckling, the buckling half wavelength is shorter than the specimen length and the buckling load associated with the short wavelength buckling is not affected by the end condition. For global column buckling however, the buckling half wavelength is equal to the length of the specimen and the buckling load associated with long wavelength buckling is affected by end conditions.

Since it was assumed that the potting produced nearly clamped conditions, the classical effective length concept was used to adjust VIPASA results to estimate global column experimental results. The effective length of a clamped

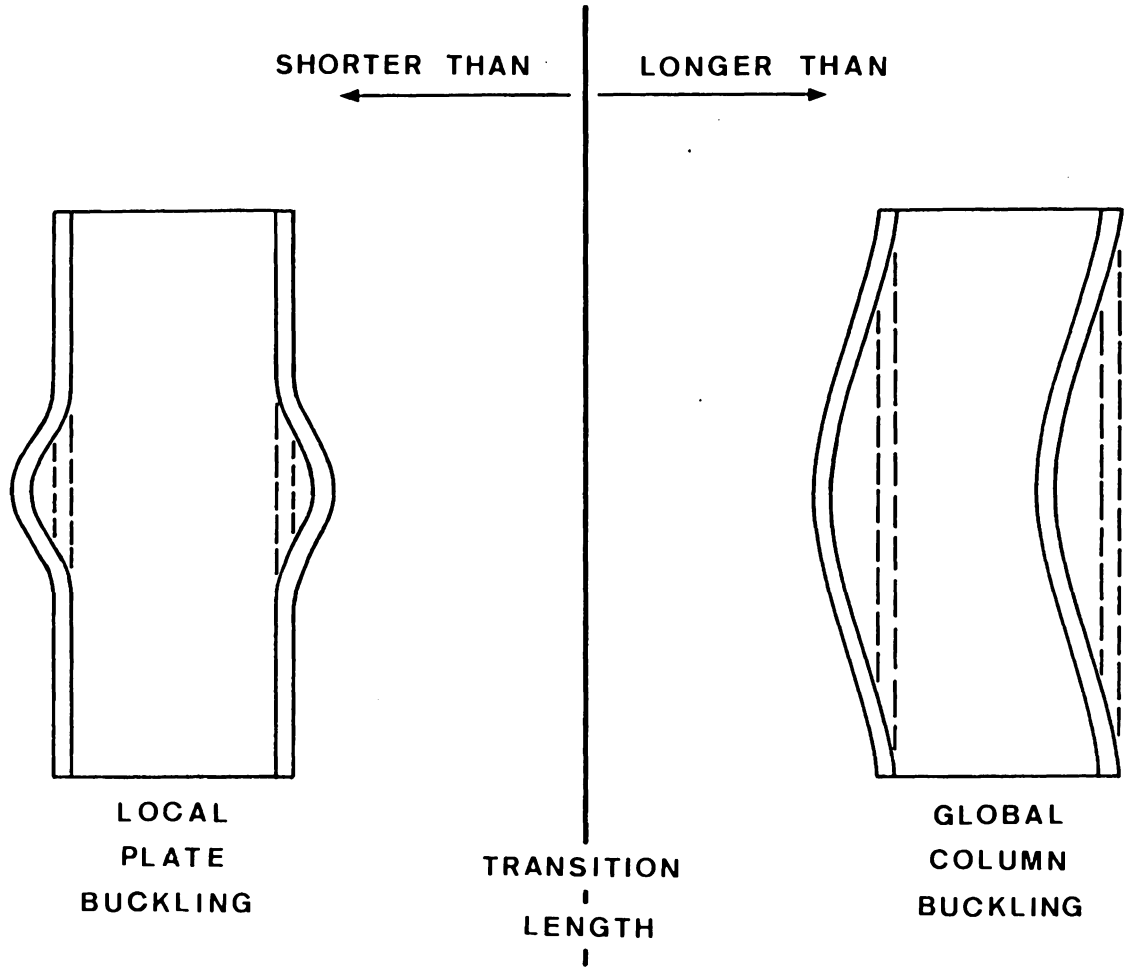

Figure 4: Behavioral Effect of Transition Length

column is one-half its actual length, and the effective length of a simply supported column is equal to its actual length (see Figure 5). Therefore, global column buckling loads predicted by VIPASA (with simple support boundary conditions) were associated with experimental specimens (almost clamped) that were twice as long as the analytical model. The results of this approach are discussed later in more detail.

2.2 INSTRUMENTATION

Electrical resistance strain gages were mounted on all specimens (see Figure 6). Arranging the gages in back-to-back pairs made it possible to determine membrane and bending strain distributions along the cross section at all load levels. Back-to-back strain gage pairs also made it possible to detect buckling. At buckling the load versus strain plots of back-to-back gages diverged from one another when bending due to buckling occurred.

Direct current displacement transducers (DCDTs) were also used with each specimen. The DCDTs were reusable, unlike the electrical resistance strain gages, and were placed at various positions around the specimen (see Figure 7). DCDTs were positioned at web centers and flange centers to detect lateral deflection caused by buckling, and one was also

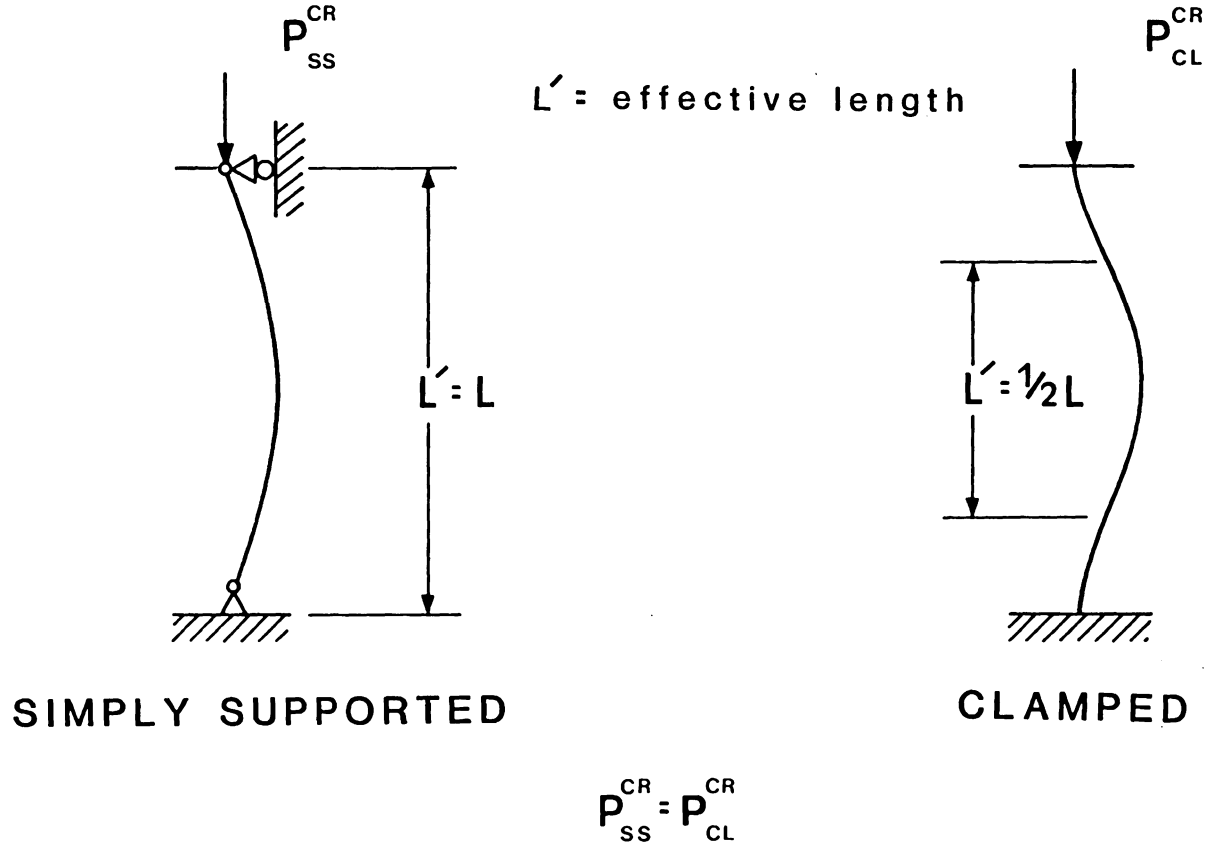

Figure 5: Definition of Effective Length

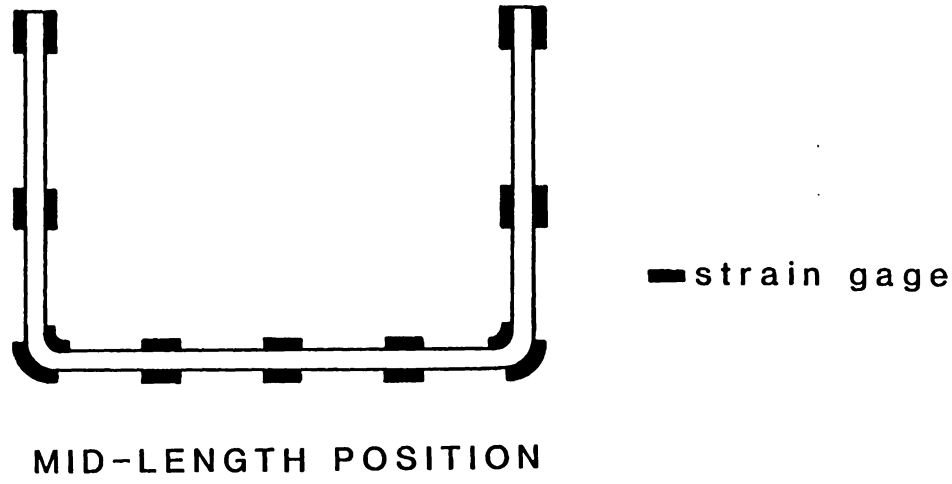

Figure 6: Back-to-Back Strain Gage Pattern

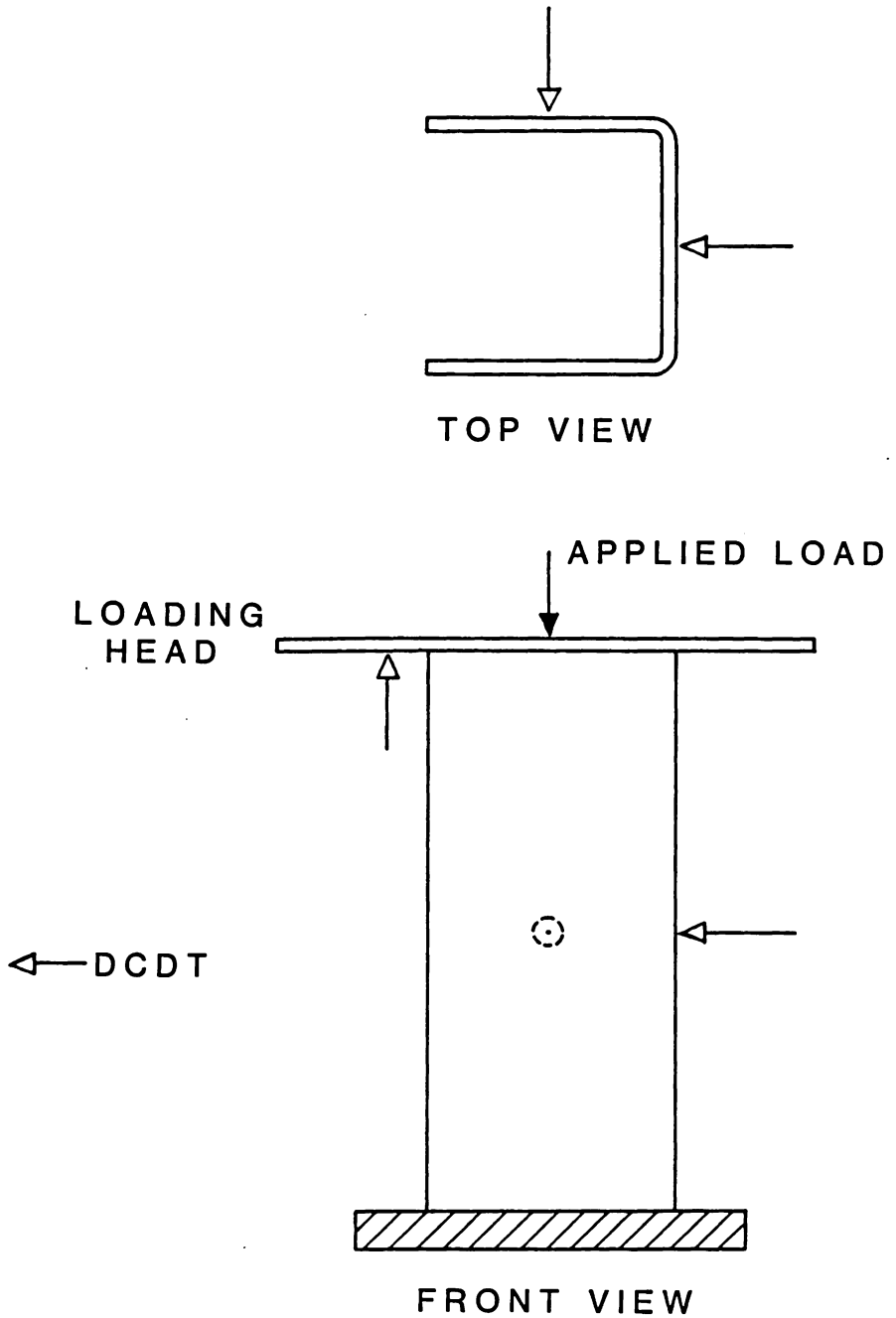

Figure 7: Direct Current Displacement Transducer (DCDT) Location

placed on the loading head to measure end shortening of the specimen.

Moiré interferometry was used to observe the buckle pattern along the front flange of the specimen (see Figure 8). The fringes represent constant out-of-plane deflection contours and were used for qualitative analysis only.

2.3 EXPERIMENTAL PROCEDURE

The procedure for a typical test was as follows. The test article was placed in the center of the loading area of a 120-kip loading machine. The loading head on the machine was adjustable to provide uniform load introduction. The lead wires from four strain gages were connected to volt meters and the specimen was loaded to approximately 10% of its predicted buckling load. While maintaining 10% of the buckling load, the loading head was adjusted until all four volt meters registered equal values, indicating a uniform strain distribution and a uniform load distribution. The specimen was then completely unloaded and the strain gage and DCDT leads were connected to a Beckman data acquisition system. Oscilloscopes were also used to monitor up to eight strain gage channels during testing. The data channels were zeroed to correspond to the zero load condition. Next a digital volt meter was calibrated to indicate applied load

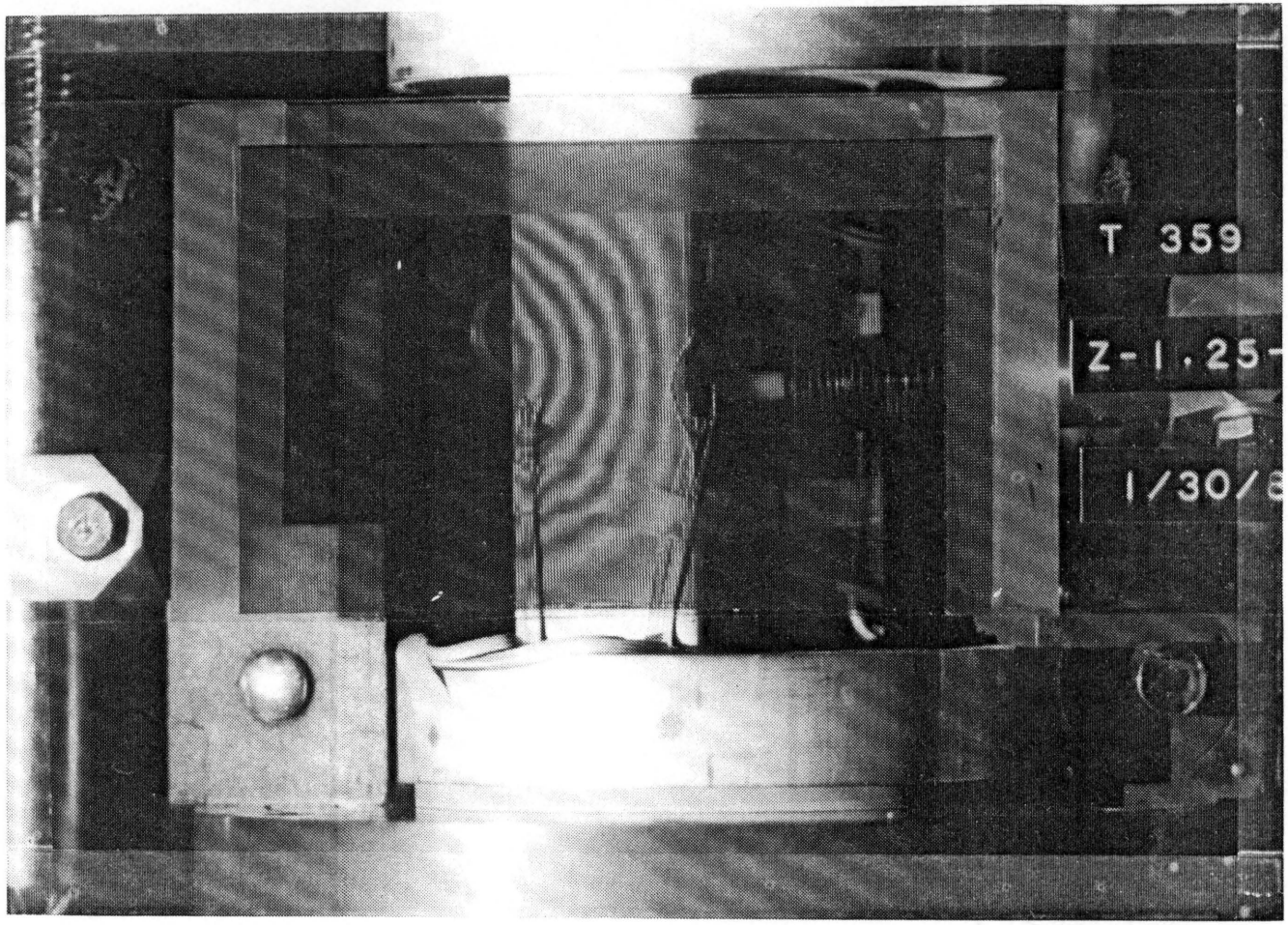

Figure 8: Moiré Fringe Pattern on Loaded Specimen

and was placed by the specimen. Next the moiré interferometry apparatus was set-up (see Figure 9). A plexiglass grid was positioned in front of the specimen and a light source was used to illuminate the specimen's front flange which was painted white. The lighting intensity and position of the volt meter were checked through the laboratory camera. When the lighting intensity and volt meter positioning were correct, the loading rate of the machine was set and the test was ready to begin. Figures 10 and 11 show the experimental apparatus. Figure 10 shows the loading machine, control panel with an ungaged specimen, digital volt meter, and DCDTs placed in the loading area. To the left of the loading machine is the console containing the oscilloscopes. Figure 11 shows a close-up of a specimen in the loading area in Figure 10. The specimen was slowly loaded, under displacement control, and photographs were taken throughout the experiment in order to record buckle patterns at various load levels. All specimens were tested to failure.

2.4 EXPERIMENTAL LOAD-SHORTENING CURVES

For each test, a plot of load, P , vs. end shortening, u, was made in order to investigate the global behavior of each specimen. The plots of P vs. u were normalized to $\frac{P}{(EA)_{eff}}$ vs. $\frac{u}{L}$ plots in order to present the results of more than one test on one set of axes.

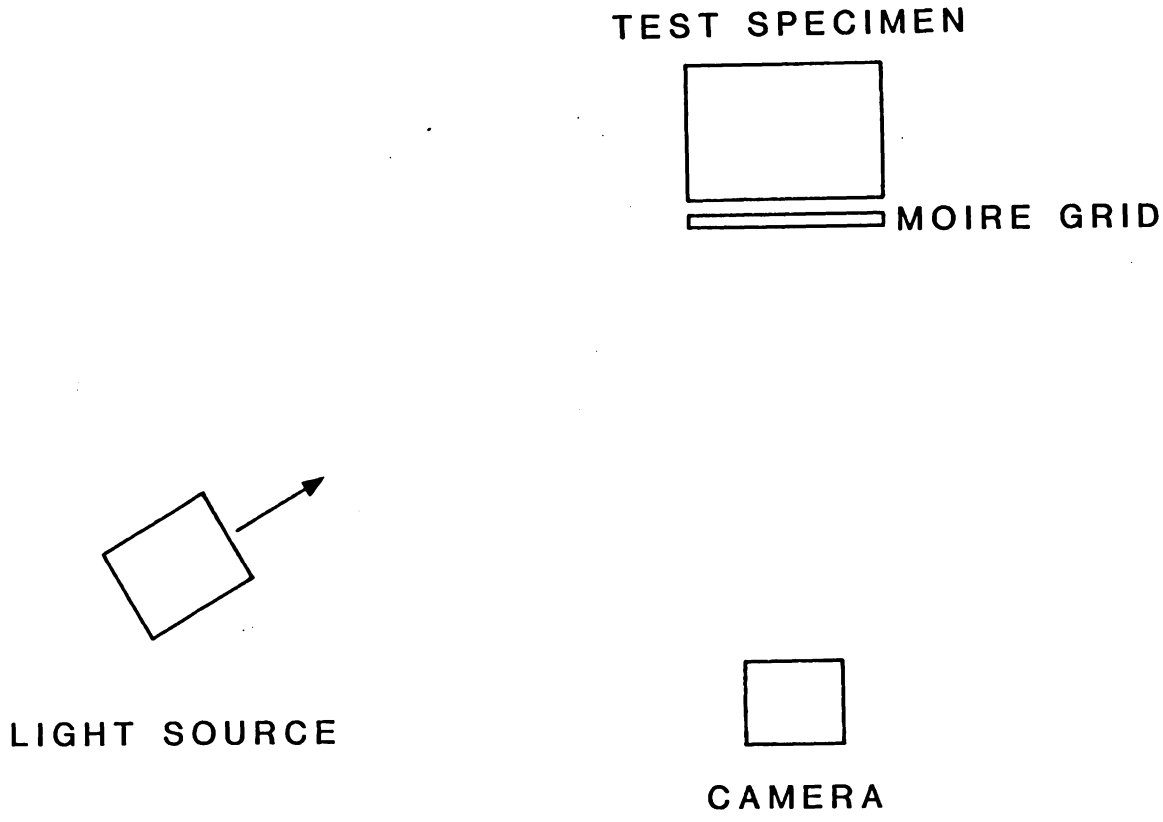

Figure 9: Schematic of Moire Interferometry Arrangement

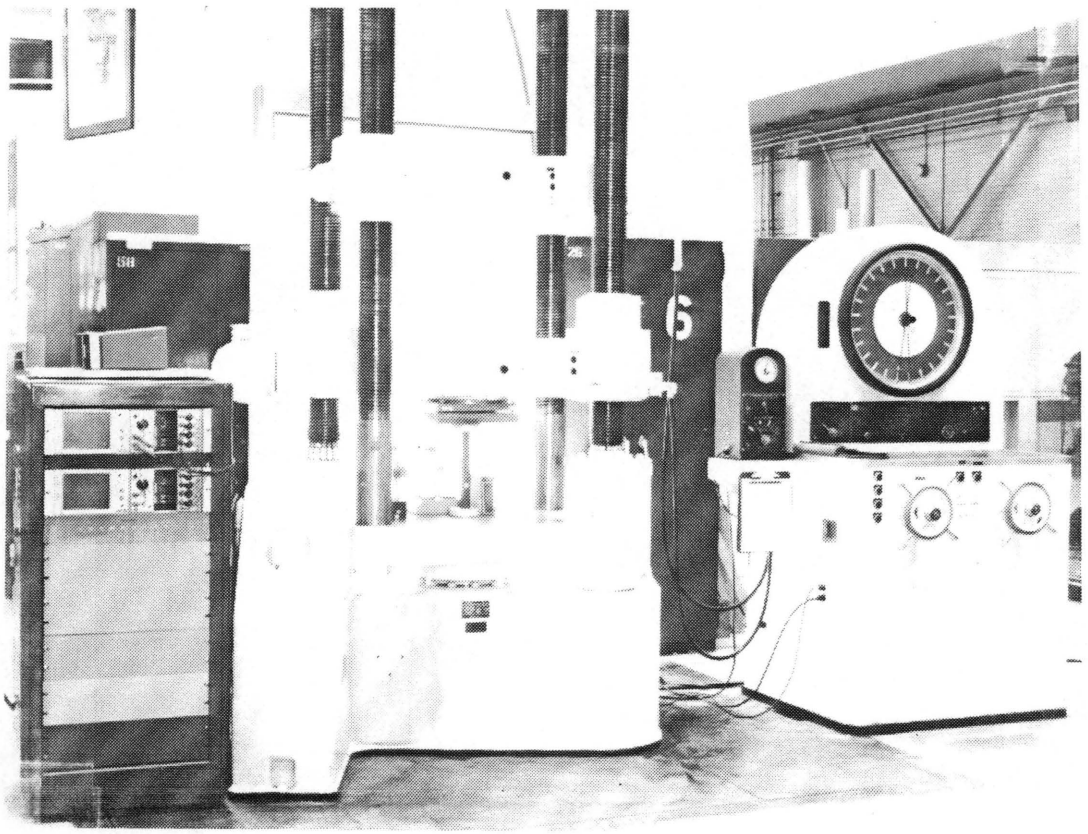

Figure 10: Experimental Apparatus

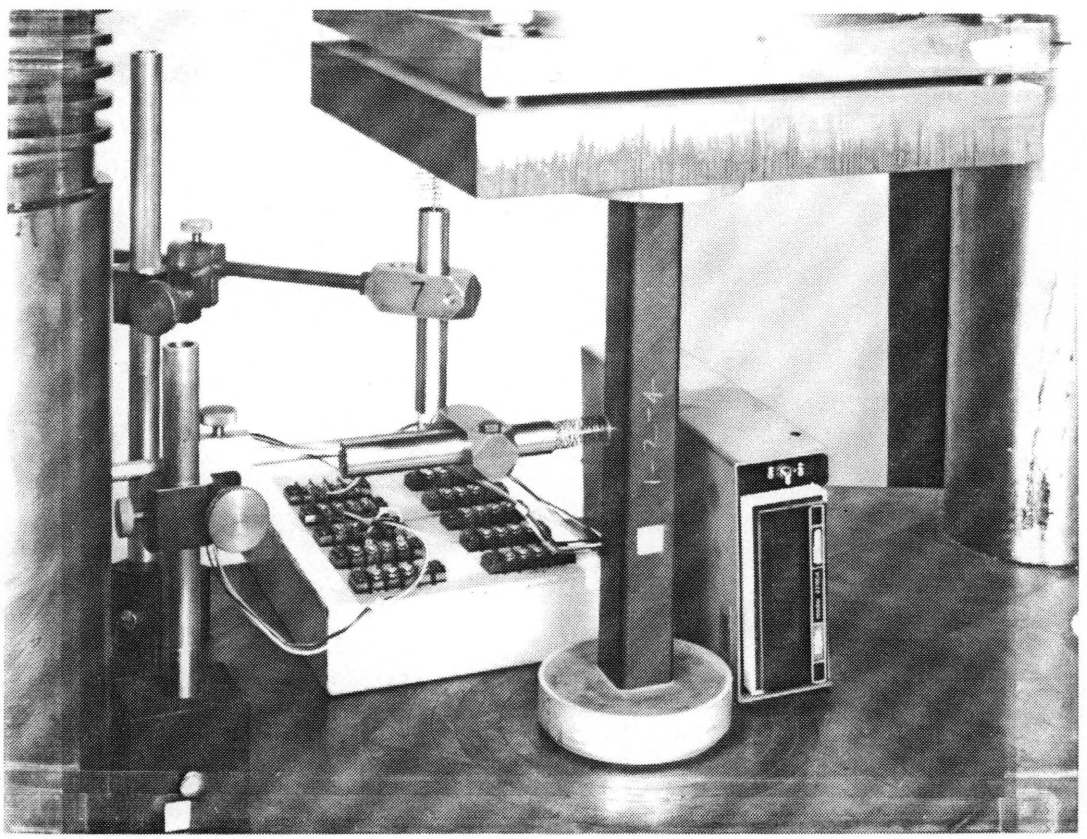

Figure 11: Close-up of Specimen in Loading Area

For each load end-shortening plot, the slope of the linear prebuckling path was determined. Then the strength of materials relationship for load and linear elastic extension (or compression) was used. The relationship being,

$$u = \frac{PL}{(EA)_{eff}} \quad . \tag{10}$$

Inverting equation (10), gives

$$P = \frac{(EA)_{eff}\, u}{L} \quad , \tag{11}$$

where u is end shortening, $(EA)_{eff}$ is the effective extensional stiffness of the specimen, and L is the length of the specimen. The slope of the P vs. u plot then was theoretically the quantity $\frac{(EA)_{eff}}{L}$. The slope was then multiplied by the exposed specimen length (excluding potting), L, in order to determine the quantity $(EA)_{eff}$ which was used to normalize the applied load P.

Manipulating equation (10) gives,

$$\frac{P}{(EA)_{eff}} = \frac{u}{L} \quad . \tag{12}$$

This indicates that theoretically, a $\frac{P}{(EA)_{eff}}$ vs. $\frac{u}{L}$ plot of a specimen exhibiting linear elastic behavior should have

a slope of one along its linear elastic prebuckling path. Figures 12-16 show the normalized load-shortening data for zee and channel specimens. All the figures show the characteristic prebuckling slope equal to one.

Based on the load-shortening curves the specimens were arranged into four groups. Tables 1 and 2 show which specimens fell into each of the four categories and the value of $(EA)_{eff}$ for each specimen. In chapter IV, more discussion and more data will be presented in support of the categorization of the four groups discussed in this section.

The first group exhibited local plate buckling behavior. The load-shortening curves associated with specimens in this group show the familiar plate postbuckling characteristics (see Figures 12 and 13). The postbuckling path begins when slope of the the load-shortening curve is reduced at buckling. The postbuckling slope remains less than one and greater than zero, and gradually decreases all the way to failure. This group includes 17 specimens (see Table 1).

The second group exhibited global column buckling behavior. This included three channel specimens that buckled in a global column mode where torsional and strong-axis rotations were coupled, and one zee specimen that buckled by bending about the weak axis (see Table 2). The geometric parameters associated with column buckling are shown in Figure 17.

TABLE 1

Group 1 -- Local Plate Buckling Specimens

SPECIMEN	NUMBER	$(EA)_{eff}$ (lbs. * 10^5)
C-1.25-1/8-.04-17.5	1-1	14.36
C-1.25-1/8-.04-18.0	1-2	14.31
C-1.25-1/8-8-3.0	1-3	6.847
C-1.25-1/8-8-4.0	1-4	8.941
C-1.25-1/4-8-4.0	1-5	8.364
C-1.25-1/8-8-18.0	1-6	9.796
C-1.25-1/8-16A-4.0	1-7	14.04
C-1.25-1/8-16B-4.0	1-8	18.68
C-0.75-1/8-8-12.0	1-9	7.731

SPECIMEN	NUMBER	$(EA)_{eff}$ (lbs. * 10^5)
Z-1.25-1/8-.04-25.0	1-10	13.85
Z-1.25-1/4-8-3.0	1-11	7.492
Z-1.25-1/8-8-4.0	1-12	8.565
Z-1.25-1/4-8-4.0	1-13	8.117
Z-1.25-1/4-8-23.0	1-14	10.52
Z-1.25-1/8-16A-4.0	1-15	14.61
Z-1.25-1/8-16B-4.0	1-16	20.28
Z-1.25-1/4-8-15.0	1-17	7.661

TABLE 2

Specimens in Groups Two, Three, and Four

GROUP 2 -- GLOBAL COLUMN BUCKLING SPECIMENS

SPECIMEN	NUMBER	$(EA)_{eff}$ (lbs. * 10^5)
C-1.25-1/8-16A-19.0	2-1	20.31
C-1.25-1/8-16B-19.0	2-2	25.77
C-0.75-1/8-16A-12.0	2-3	13.53
Z-0.75-1/8-16A-15.0	2-4	13.81

GROUP 3 -- MATERIAL SHORT COLUMN SPECIMENS

SPECIMEN	NUMBER	$(EA)_{eff}$ (lbs. * 10^5)
C-0.75-1/8-16A-4.0	3-1	9.800
Z-0.75-1/8-16A-4.0	3-2	10.44

GROUP 4 -- SPECIMEN WITH AN UNSTABLE POSTBUCKLING RESPONSE

SPECIMEN	NUMBER	$(EA)_{eff}$ (lbs. * 10^5)
Z-1.25-1/8-16A-24.0	4-1	19.83

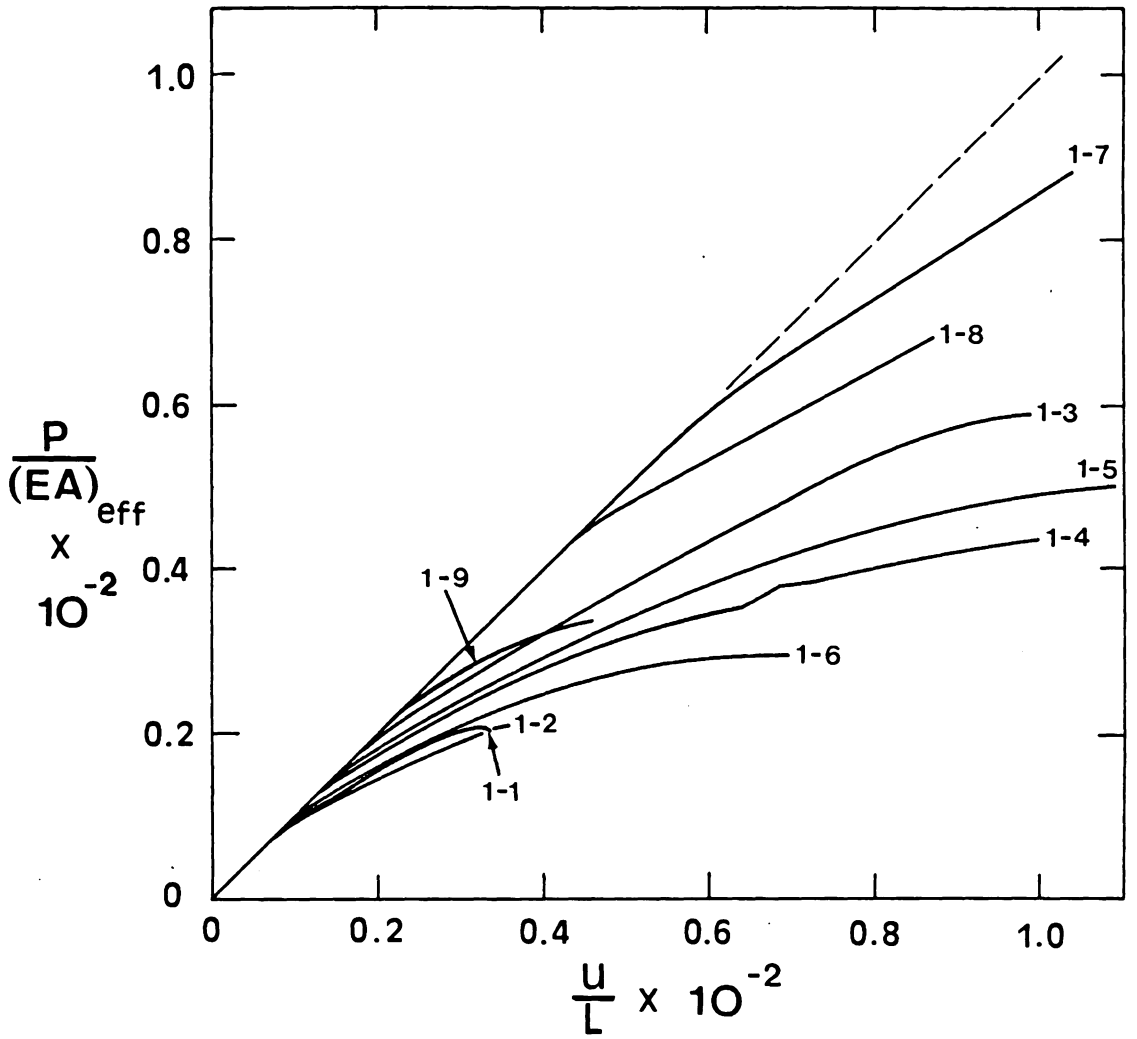

1-1 C-1.25-1/8-.04-17.5
1-2 C-1.25-1/8-8-.04-18.0
1-3 C-1.25-1/8-8-3.0
1-4 C-1.25-1/8-8-4.0
1-5 C-1.25-1/4-8-4.0
1-6 C-1.25-1/8-8-13.0
1-7 C-1.25-1/8-16A-4.0
1-8 C-1.25-1/8-16B-4.0
1-9 C-0.75-1/8-8-12.0

Figure 12: Load-Shortening Curves for Channel Sections in Group 1

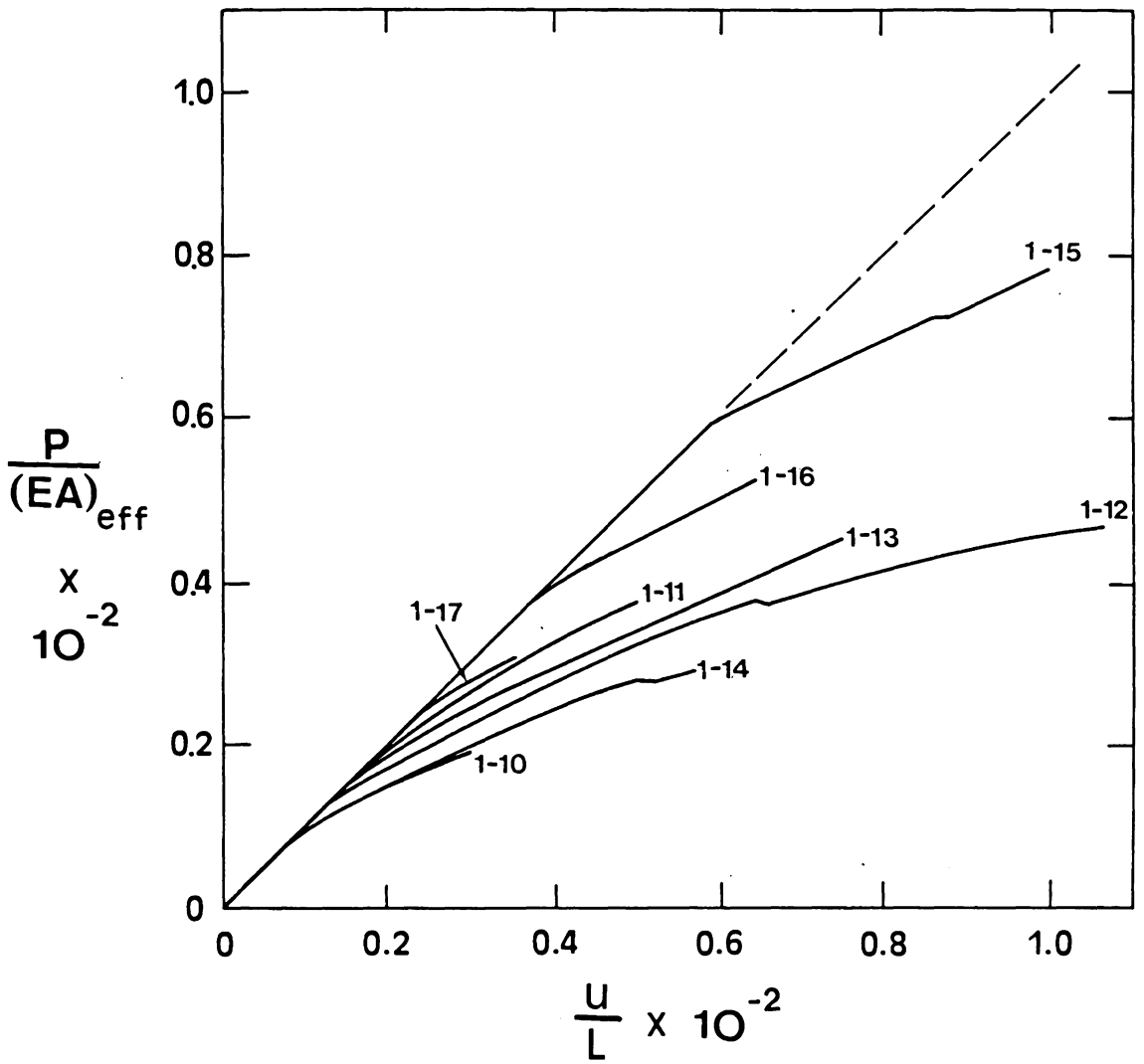

1-10	Z-1.25-1/8-.04-25.0	1-14	Z-1.25-1/4-8-23.0
1-11	Z-1.25-1/4-8-3.0	1-15	Z-1.25-1/8-16A-4.0
1-12	Z-1.25-1/8-8-4.0	1-16	Z-1.25-1/8-16B-4.0
1-13	Z-1.25-1/4-8-4.0	1-17	Z-0.75-1/4-8-15.0

Figure 13: Load-Shortening Curves for Zee Sections in Group 1

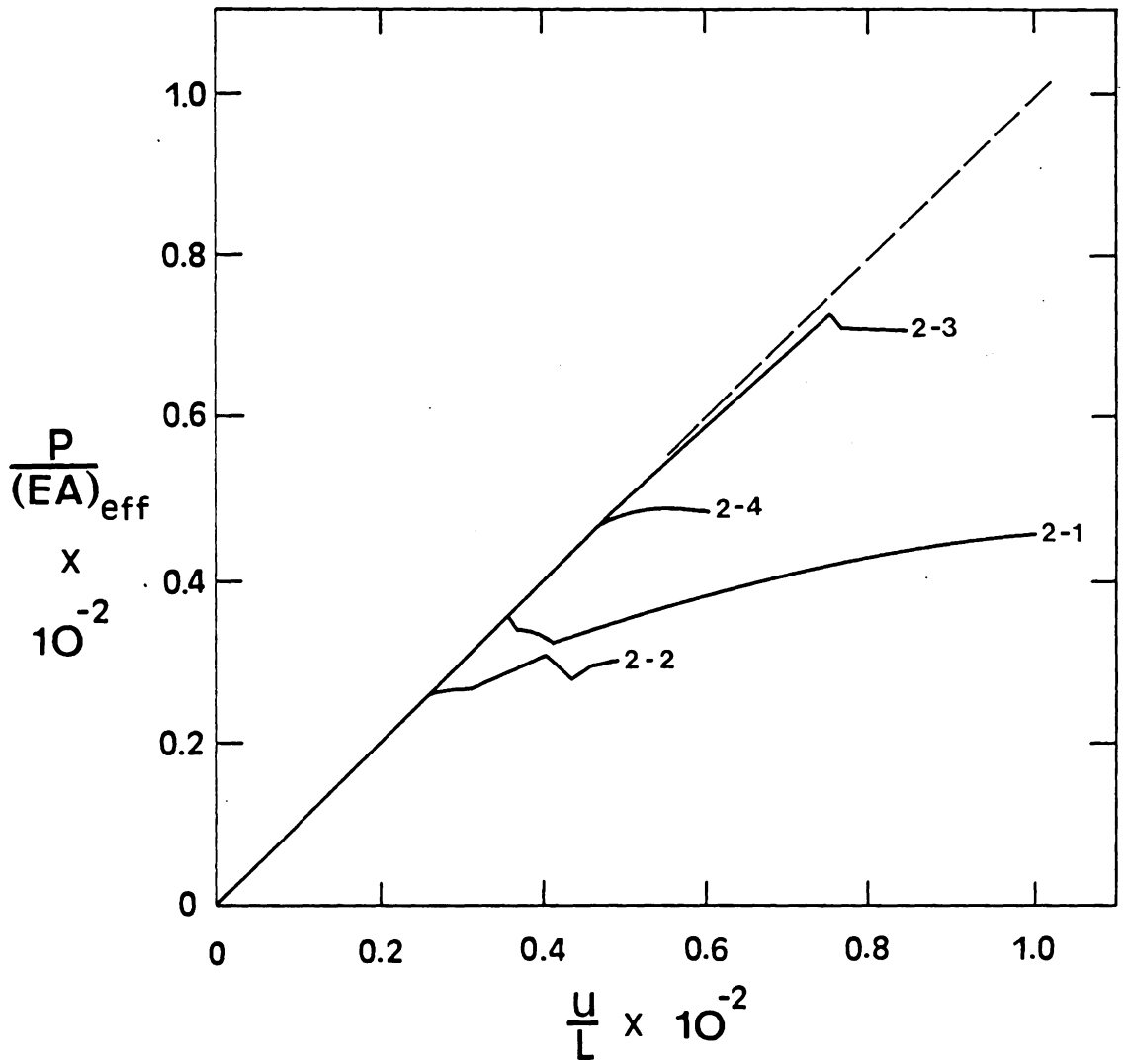

2-1 C-1.25-1/8-16A-19.0
2-2 C-1.25-1/8-16B-19.0
2-3 C-0.75-1/8-16A-12.0
2-4 Z-0.75-1/8-16A-15.0

Figure 14: Load-Shortening Curves for Group 2

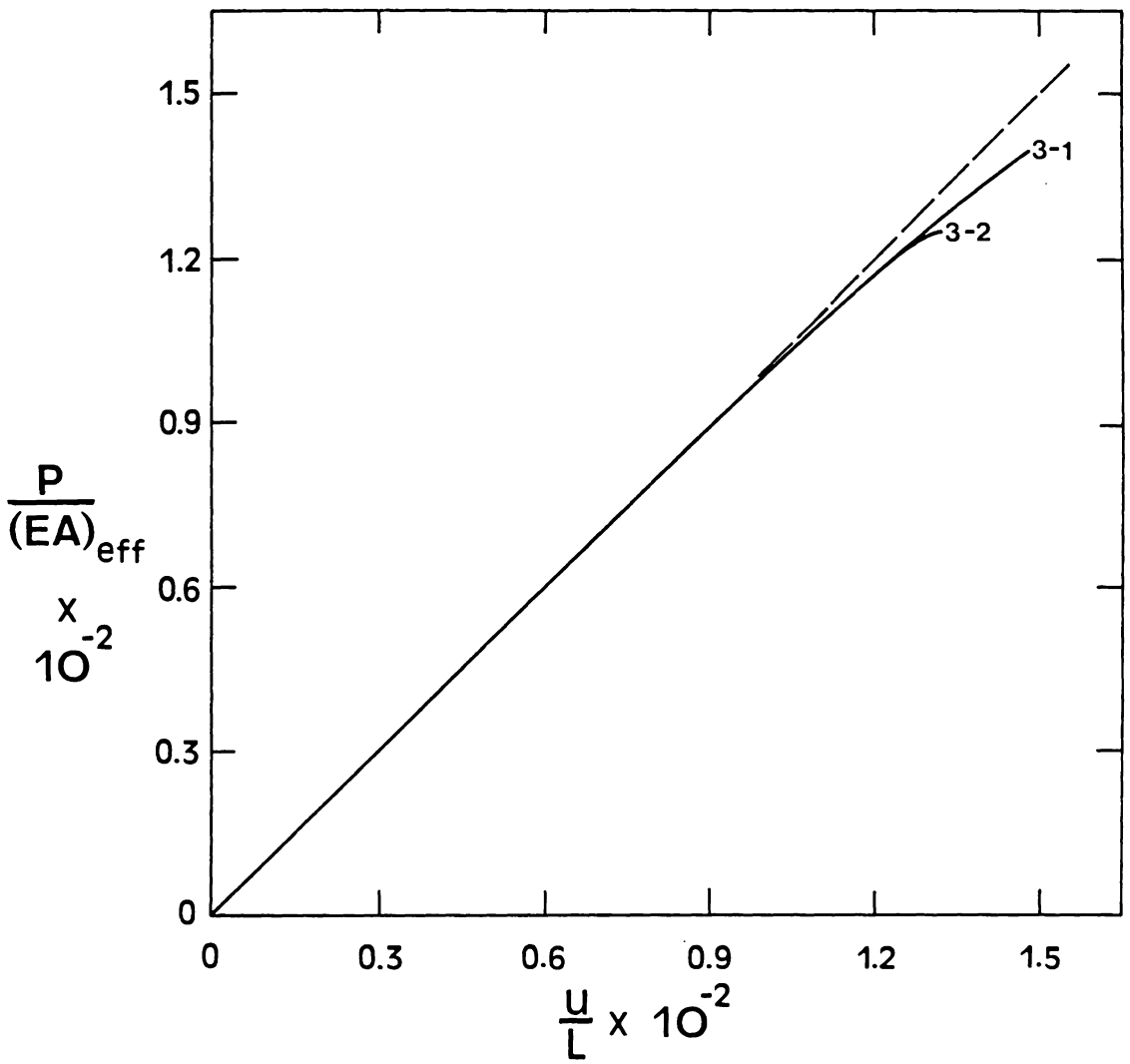

3-1 C-0.75-1/8-16A-4.0 3-2 Z-0.75-1/8-16A-4.0

Figure 15: Load-Shortening Curves for Group 3

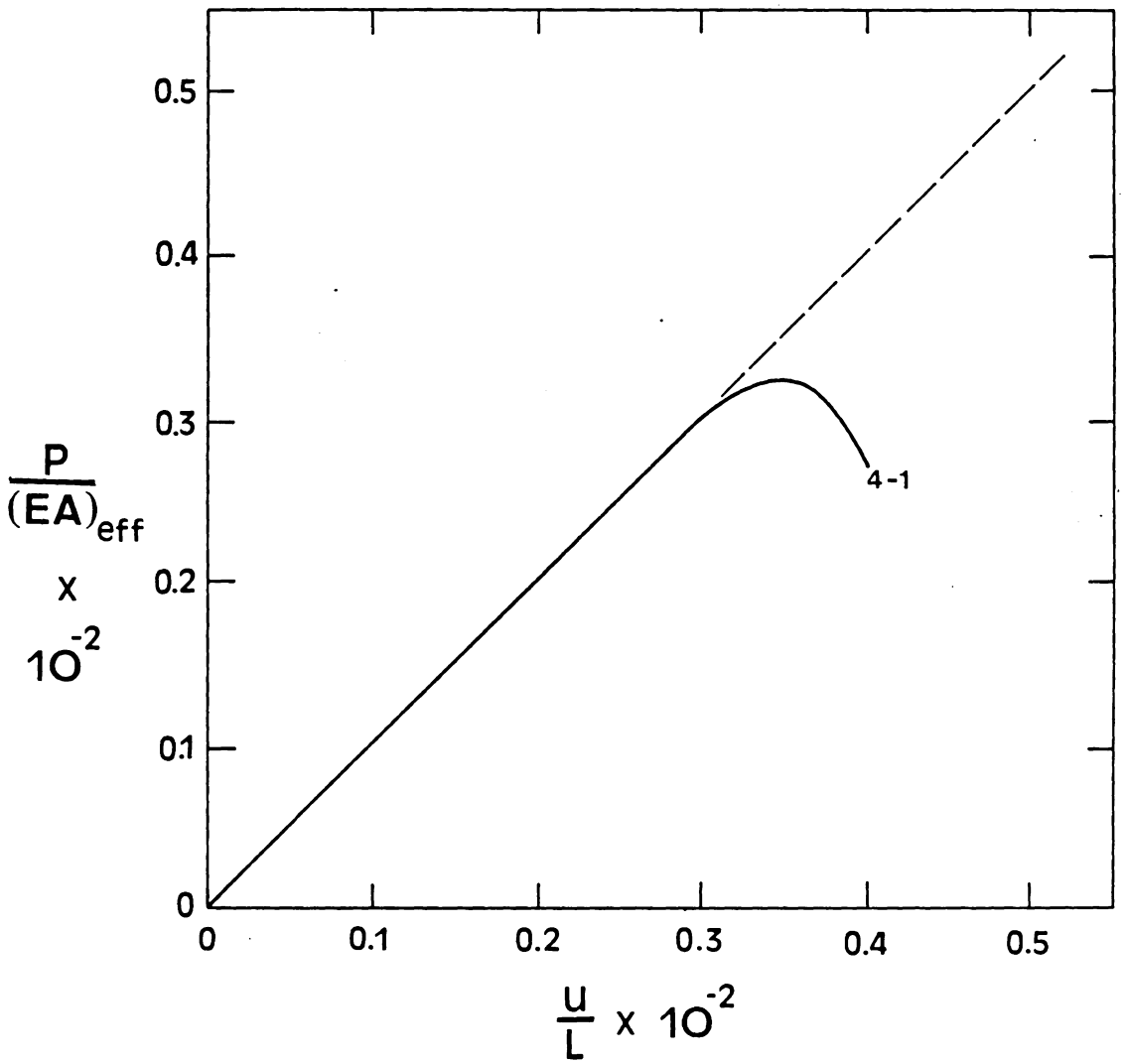

4-1 Z-1.25-1/8-16A-24.0

Figure 16: Load-Shortening Curves for Group 4

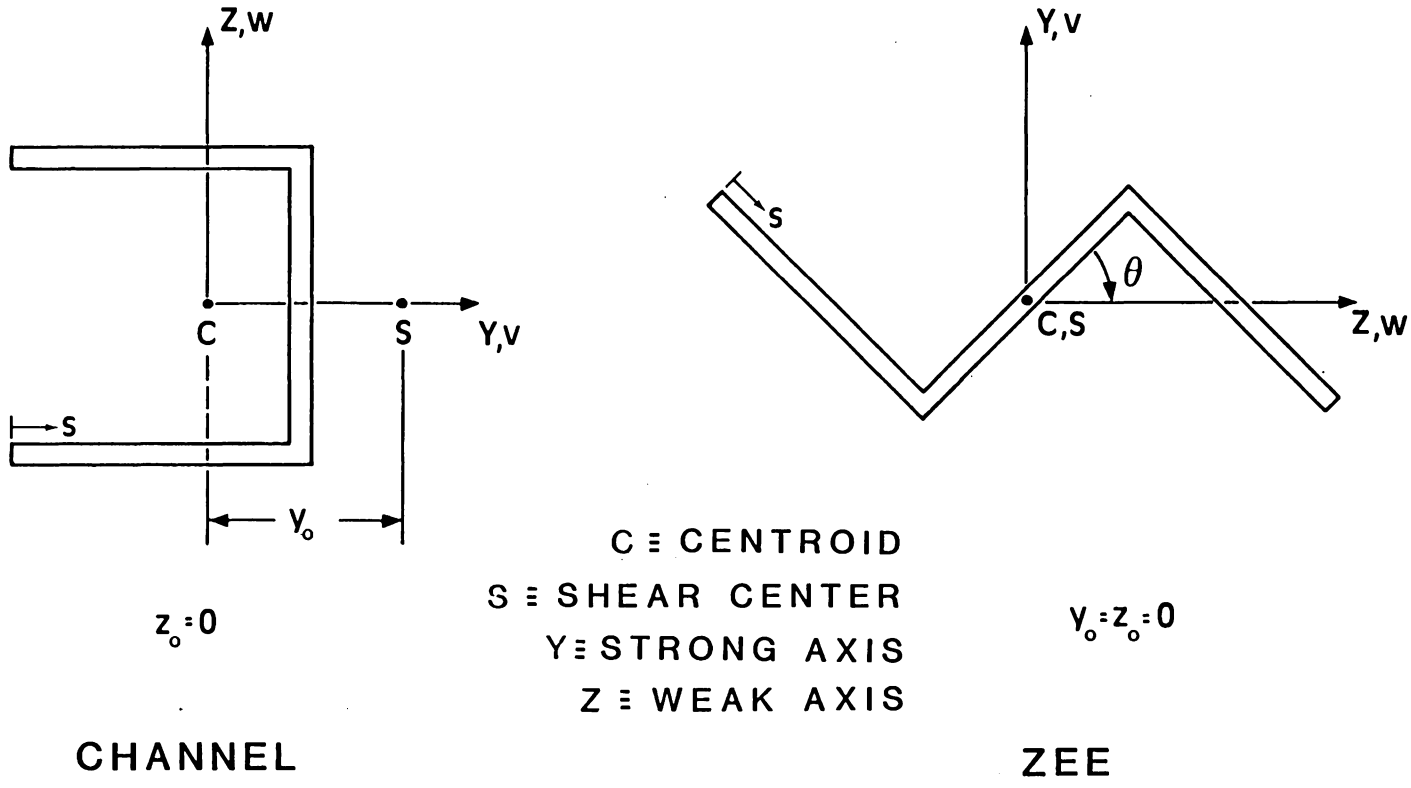

Figure 17: Geometric Parameters Associated with Column Buckling

The load-shortening curves associated with these specimens show the familiar column postbuckling characteristics, namely a postbuckling slope of zero (see Figure 14). For the zee specimen, 2-4 in Figure 14, the postbuckling slope of zero is clearly evident. For the channel specimens, 2-1 to 2-3 in Figure 14, the postbuckling paths were erratic, but generally followed a horizontal (slope = 0) direction. It is suspected that the erratic behavior of the channel postbuckling paths reflected gradual local damage and internal load redistribution that occurred as the channel twisted in the torsional mode.

The third group exhibited a material nonlinear response prior to buckling and failed at the buckling load. Thus the deviation from the prebuckling equilibrium path in Figure 15 for specimens 3-1 and 3-2 is due to softening of the material. Notice that this occurs at approximately 1% strain which is, in general, close to the failure strains for this material system. This behavior for graphite-epoxy is analogous to the short column response for ductile metals which buckle at stress levels exceeding the proportional limit. Hence this group will be described as exhibiting material short column behavior. This group includes one zee specimen and one channel specimen that had flange widths of 0.75 inches, stacking sequences of type 16A, and 4 inches of

exposed length between the potted ends (see Table 2). The two specimens differed only by the relative orientations of their two flanges.

The fourth group is actually just one zee specimen (number 4-1). It exhibited global column buckling behavior followed by plate buckling behavior of the flange on the compressive side of the weak (bending) axis. The load-shortening curve for this specimen shows unstable postbuckling characteristics (i.e. the postbuckling slope is negative, see Figure 16).

This instability was associated with the occurrence of the additional mode of deformation. The specimen originally buckled globally in a column mode and the load-shortening curve began to flatten out as did the curve for the zee specimen 2-4 in Figure 14. For specimen 4-1, however, after bending around the weak axis occurred, the flange with its free edge on the compressive side of the weak axis buckled in a plate mode. This additional mode softened the structure, which had already buckled like a column, and caused it to collapse. This collapse is reflected by the negative postbuckling slope.

Chapter III

BUCKLING

3.1 INITIAL BUCKLING CALCULATIONS

Preliminary buckling calculations made with VIPASA involved material property values that were generally accepted for the AS4-3502 material system and 2024-T3 aluminum. Since the initial prediction of a buckling load served as only a rough guide for selecting the loading range for each test, the generally accepted material properties were satisfactory for this purpose. The properties used in the preliminary buckling calculations are shown in Table 3. Table 3 also shows other material properties used in later calculations of "corrected" buckling loads. These new properties were found in a qualification report prepared by General Dynamics Fort Worth for Hercules Incorporated [12]. The fiber and matrix moduli were determined from a quality assurance certification by Hercules Incorporated [13].

As discussed earlier, there was a difference between analytical boundary conditions (simply supported) and experimental potted boundary conditions (clamped). The local buckling load was assumed to be unaffected by end conditions. For global buckling cases the analytical (simply supported) load was assumed to correspond to a clamped specimen twice as long as the analytical model.

TABLE 3

Material Properties Used in Buckling Calculations

PRELIMINARY (OLD)	FINAL (NEW)
$E_1 = 18.5*10^6$ psi.	$E_1 = E_f*v_f + E_m*(1-v_f)$
$E_2 = 1.64*10^6$ psi.	$E_f = 33.0*10^6$ psi.
$G_{12} = 0.87*10^6$ psi.	$E_m = 1.33*10^6$ psi.
$\nu_{12} = 0.300$	$E_2 = 1.51*10^6$ psi.
	$G_{12} = 0.844*10^6$ psi.
	$\nu_{12} = 0.331$

3.2 MATERIAL PROPERTY ADJUSTMENT

In order to achieve better agreement between predicted and experimental buckling loads, the material properties E_1 (for composite specimens) and E (for aluminum specimens) used in VIPASA were adjusted to match values indicated by experimental linear prebuckling paths. In the prebuckling range, the specimens exhibited pure compression and no bending. By assuming that the cross section can be unfolded into a flat plate, the inplane loading can be represented by the following formulation,

$$\begin{Bmatrix} N_x \\ N_y \\ N_{xy} \end{Bmatrix} = \begin{bmatrix} A_{11} & A_{12} & A_{16} \\ A_{12} & A_{22} & A_{26} \\ A_{16} & A_{26} & A_{66} \end{bmatrix} \begin{Bmatrix} \varepsilon_x \\ \varepsilon_y \\ \gamma_{xy} \end{Bmatrix} \tag{13}$$

where $\{N\}$ are the membrane stress resultants, $[A]$ are the laminate extensional stiffnesses, and $\{\varepsilon\}$ are the in-plane strains. For a more detailed discussion, see Jones [14]. By assuming that N_y and N_{xy} equal zero for the testing condition, and since A_{16} and A_{26} equal zero for balanced laminates (i.e. for every θ ply there is a $-\theta$ ply of equal thickness), equation (13) becomes,

$$\begin{aligned} N_x &= A_{11}\varepsilon_x + A_{12}\varepsilon_y \\ 0 &= A_{12}\varepsilon_x + A_{22}\varepsilon_y \end{aligned} \tag{14}$$

Solving the second equation for ε_y, and substituting the expression for ε_y into the first equation, results in

$$N_x = A_{11}^* \varepsilon_x \quad , \tag{15}$$

where

$$A_{11}^* = A_{11} - \frac{A_{12}^2}{A_{22}} \quad . \tag{16}$$

Multiplying equation (15) by $b = 2b_f + b_w$, produces the equation

$$P = A_{11}^* b\varepsilon_x \quad . \tag{17}$$

Equation (17) is in a form that can be easily used with experimental load and strain data. It indicates that the slope of a P versus ε_x plot is the quantity $A_{11}^* b$ (see Figure 18). Since b is known, the slope of the linear prebuckling portion of a P versus ε_x plot gives the value A_{11}^* that is required .

Equation (17) is similar to equation (11) of Section 2.4. They are both load-deflection equations. It is important to note, however, that the quantity $(EA)_{eff}$ in equation (11) is not equal to $A_{11}^* b$ in equation (17). $(EA)_{eff}$ was determined from a load-shortening (P vs. u) curve and reflects the overall behavior of the structure. In contrast, $A_{11}^* b$ was determined from a load-strain (P vs. ε_x) curve associated with axial strain of the web center and reflects the local behavior of the material at that position. This is why

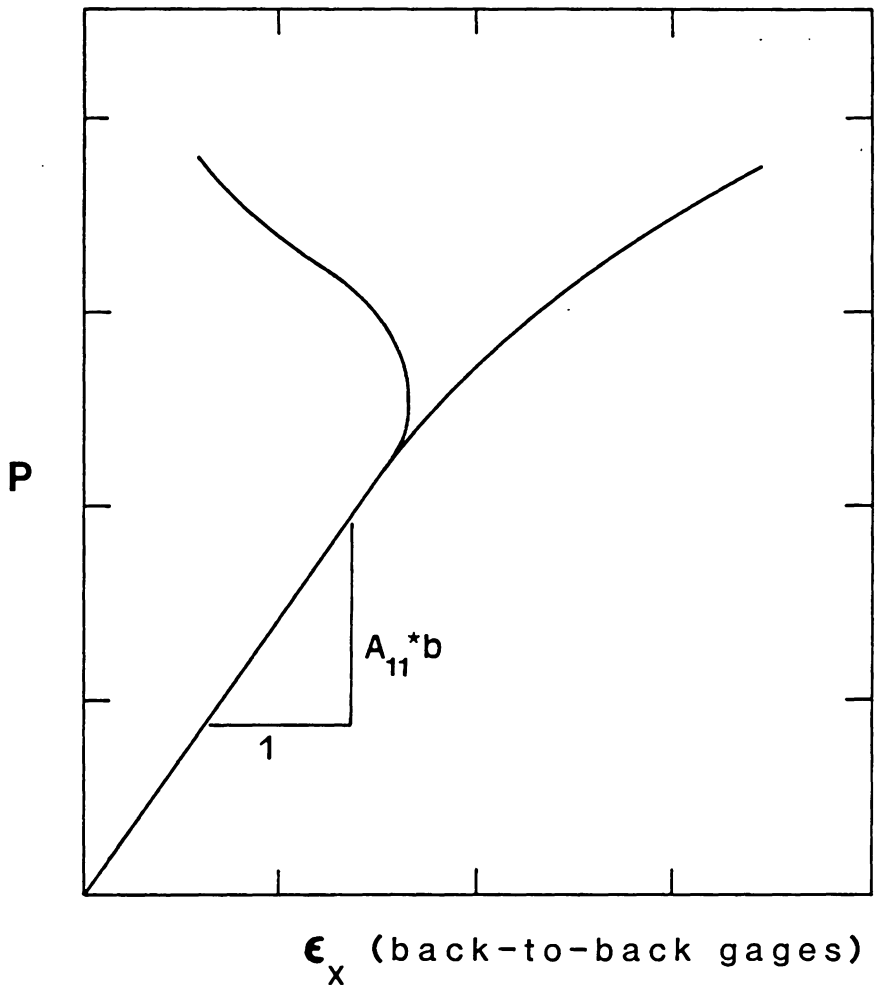

Figure 18: Experimental Determination of A_{11}^*

material property adjustments were made based on $A_{11}^{*}b$ and not on $(EA)_{eff}$.

For each test, a plot of P versus ε_x for each of the back-to-back strain gages at the center of the web was made. From the plots, a range of linear prebuckling behavior was determined. In this linear range of data, four data points of the form $(x,y)=(\varepsilon_x,P)$ were selected. The ε_x value used for each data point was determined by averaging the back-to-back gage data. This average strain did not differ significantly from the surface strains since there was little bending present during prebuckling. A linear regression analysis was performed on the four data points to determine the slope of a straight line passing most closely through the data. This slope was the $A_{11}^{*}b$ value of interest. By dividing by the developed width of the cross section ($b=2b_f+b_w$), the A_{11}^{*} value of interest was then determined.

With the experimental A_{11}^{*} value determined, laminate analysis is used to relate A_{11}^{*} to the in-plane lamina material properties (E_1, E_2, ν_{12}, and G_{12}) and nominal lamina thickness, t. First, it was assumed that the lamina fiber direction modulus E_1 was the dominant material property associated with buckling behavior. Therefore, E_1 was the only variable material property and E_2, ν_{12}, and G_{12} were assumed constant. The variation in E_1 was assumed to

be a result of a variation in fiber volume fraction, v_f, from specimen to specimen. The modulus E_1 varies with v_f according to the rule of mixtures,

$$E_1 = v_f E_f + (1-v_f) E_m \tag{18}$$

where E_f and E_m are the fiber modulus and matrix modulus respectively. The moduli E_f and E_m were assumed constant. From equation (16) A_{11}^* is a function of the extensional stiffnesses A_{11}, A_{12}, and A_{22}. From laminate analysis, see Reference [14] for example, the extensional stiffnesses are functions of lamina material properties and nominal ply thickness. Since E_1 was the only variable material property, the extensional stiffnesses for a specified laminate were functions of E_1 only. Since E_1 was a function of v_f only, it follows that A_{11}^* was a function of v_f only.

A computer code was written to calculate E_1 and A_{11}^* values over a range of fiber volume fractions. Each experimental A_{11}^* value was then matched to the closest computer generated A_{11}^* value in the range. This determined the E_1 value and the v_f value that corresponded to each particular specimen. The new E_1 value was then used in VIPASA to calculate an adjusted buckling load.

For the aluminum cases, the formulation for A_{11}^* was simply,

$$A_{11}^* = Et \tag{19}$$

where E is Young's modulus and t is the wall thickness. To determine the adjusted E value, the experimental A_{11}^* value was simply divided by the wall thickness of the aluminum specimen.

3.3 ADJUSTED BUCKLING LOADS

Modeling the specimens with the code VIPASA involved joining perfect plate elements to form channel and zee specimens with right angle corners. Since the actual specimens had rounded corners with variable resin contents due to fabrication procedures, it was expected that the predicted and experimental buckling loads would not agree perfectly. It is because of these modeling discrepancies that a ±10% tolerance on the agreement between experimental and predicted buckling loads was considered acceptable.

Table 4 shows the comparison of VIPASA predicted buckling loads, P_{NEW}^{CR} and experimental buckling loads, P_{EXP}^{CR}. In group 1, four of the 17 test cases showed greater than 10% difference between experimental and predicted buckling loads. An explanation for these four specimens is not apparent.

In groups 2 and 4, in which specimens buckle in a column mode, the percentage difference between experimental and predicted buckling loads is much greater than 10%. These large discrepancies indicate that the assumptions made in

TABLE 4

Predicted and Experimental Buckling Loads

SPECIMEN	P^{CR}_{EXP} (lbs)	v_f	$E_{1_{NEW}}$ (psi)	P^{CR}_{NEW} (lbs)	Δ% wrt P^{CR}_{EXP}
Group 1					
C-1.25-1/8-.04-17.5	1210	---	10.10	1246	2.98
C-1.25-1/8-.04-18.0	1240	---	10.98	1355	9.27
C-1.25-1/8-8-3.0	1120	.520	17.80	1330	18.75
C-1.25-1/8-8-4.0	1180	.565	19.22	1194	1.19
C-1.25-1/4-8-4.0	1250	.530	18.12	1134	-9.28
C-1.25-1/8-8-18.0	920	.530	18.12	1055	14.67
C-1.25-1/8-16A-4.0	8300	.505	17.32	8208	-1.11
C-1.25-1/8-16B-4.0	8330	.540	18.43	8946	7.39
C-0.75-1/8-8-12.0	1730	.525	17.96	1970	13.87
Z-1.25-1/8-.04-25.0	1175	---	10.09	1239	5.45
Z-1.25-1/4-8-3.0	1275	.465	16.06	1218	-4.47
Z-1.25-1/8-8-4.0	1200	.560	19.07	1183	-1.42
Z-1.25-1/4-8-4.0	1160	.510	17.48	1096	-5.52
Z-1.25-1/4-8-23.0	975	.545	18.59	1072	9.95
Z-1.25-1/8-16A-4.0	8400	.500	17.17	8048	-4.19
Z-1.25-1/8-16B-4.0	7900	.565	19.22	9190	16.32
Z-0.75-1/4-8-15.0	1925	.535	18.27	1993	3.53
Group 2					
C-1.25-1/8-16A-19.0	7000	.520	17.80	7915	13.07
C-1.25-1/8-16B-19.0	6830	.535	18.27	9745	42.68
C-0.75-1/8-16A-12.0	9670	.530	18.12	13188	36.38
Z-0.75-1/8-16A-15.0	6540	.510	17.48	8789	34.39
Group 3					
C-0.75-1/8-16A-4.0	13300	.480	16.53	13264	-0.27
Z-0.75-1/8-16A-4.0	12900	.450	15.58	12437	-3.59
Group 4					
Z-1.25-1/8-16A-24.0	6310	.505	17.32	8183	29.68

Section 2.1 about the boundary conditions and effective length of the specimens were not valid. For the zee specimens, the assumed effective length of 1/2 the actual length was too short. This implies that the potting material did not produce clamped boundary conditions, which is quite understandable since perfectly clamped conditions are impossible to achieve experimentally. The effective length factor for each specimen is presented in Table 5. The factor is the ratio of the length of a simply supported column divided by the length of the actual specimen. The length of the simply supported column is the value required in the VIPASA code to equate the buckling load computed by VIPASA to the experimental buckling load.

For the channel specimens, the global buckling mode involves rotation around both the strong axis and the torsional axis of the specimen. Under these circumstances, the assumed clamped effective length of 1/2 the actual length was, again, too short. As shown in Appendix A, the theoretical effective length for a clamped specimen with coupled torsional/strong-axis global buckling is 1/2 the actual length. This fact is interesting because it indicates that the classical weak-axis buckling effective-length relationship holds for the more complicated coupled buckling mode. The channel specimens then, had the same "soft" end fixity

TABLE 5

Effective Length Factors for Global Column Specimens

SPECIMEN	FACTOR
C-1.25-1/8-16A-19.0	0.553
C-1.25-1/8-16B-19.0	0.663
C-0.75-1/8-16A-12.0	0.625
Z-0.75-1/8-16A-15.0	0.587
Z-1.25-1/8-16A-24.0	0.583

$$\text{FACTOR} = \frac{L_{PASCO}}{L_{EXP}}, \quad \text{such that } P^{CR}_{NEW} = P^{CR}_{EXP}$$

factor which increased their effective lengths just as it did for the zee specimens. The experimental effective lengths for the channel specimens are presented in Table 5 along with those for the zee specimens.

The end potting produced an end fixity uncertainty for the column specimens. The potting material was an aluminum filled epoxy based compound manufactured by Hysol. In addition to making it difficult to correct global column buckling loads, the end fixity uncertainty of the potting material caused the unexpected column behavior in groups 2 and 4. Since the experimental boundary conditions were softer than clamped, specimens designed shorter than the assumed ideal clamped transition length buckled globally in column modes because their effective lengths were in reality longer than the clamped transition length.

The results for category 3 are very good. The buckling load correction procedure was most successful for this group.

Chapter IV

POSTBUCKLING AND FAILURE

In this chapter, data will be presented that illustrates the behaviors discussed earlier. One section will be devoted to each of the groups defined in Section 2.4. In each section, one example will be presented that is representative of the behavior of all the specimens in that group. In the last section, strains along the cross section at failure for each specimen are presented in tabular form.

4.1 LOCAL PLATE BUCKLING TO FAILURE

The local plate buckling mode associated with the specimens in group 1 can be described as follows. Prior to buckling, the cross section is undeformed, with a uniform axial load distribution and zero bending load. In the postbuckling response, the corners of the cross sections remain straight while the free edges of the flanges and the center of the web bend the greatest amount (see Figure 19). In this configuration, the straight corners are in axial compression while the free edges of the flanges and the center of the web are in combined bending and compression. As the applied axial load increases the bending in the postbuckling response increases significantly with respect to the membrane compression in the flanges and center of the web.

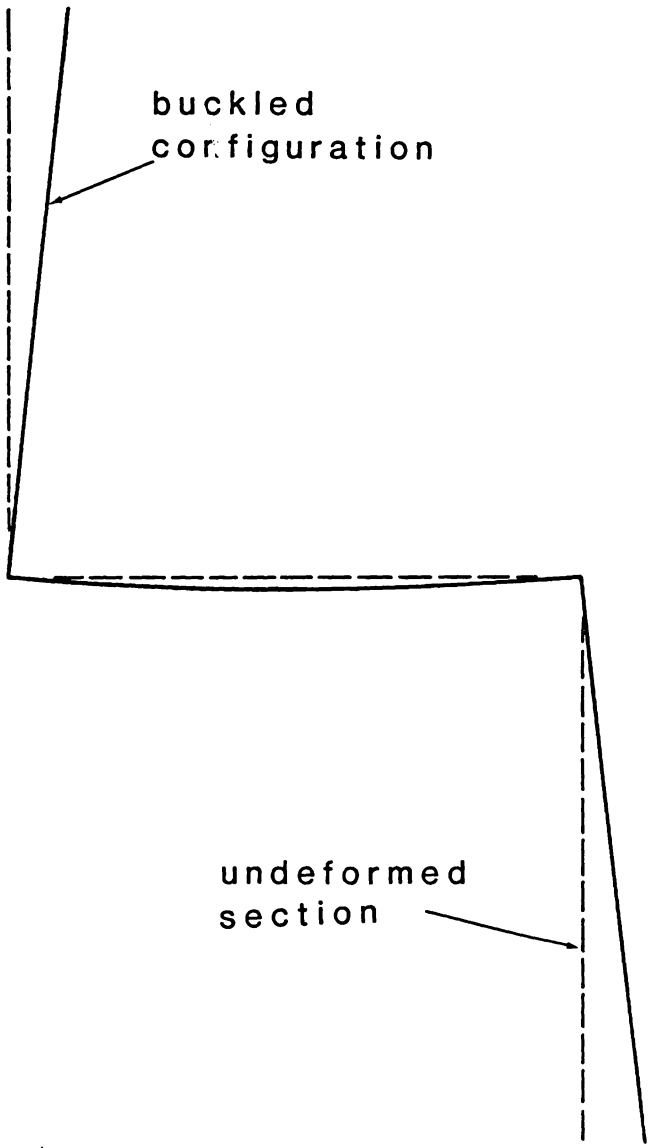

Figure 19: Local Plate Buckling Mode

This situation is shown in Figures 20 and 21. Figure 20 shows the experimental membrane strain distributions and Figure 21 shows the experimental bending strain distributions for specimen 1-13 at four different load levels. At the prebuckling load levels the membrane strain is uniform and the bending strain is close to zero. At the postbuckling load levels, Figure 20 shows peaks at the corner locations. These peaks represent the concentration of axial load into the corners which remain straight. The postbuckling distributions in Figure 21 show peaks at the free edges of flanges and at the center of the web. These peaks represent the bending of the flanges and web as expected.

The failure of specimens in group 1 involved cracking and delamination across the cross section. Figures 22 and 23 show the zee specimen 1-13 after failure. There is cracking at the midlength position that appears to be more pronounced in the corners. Both free edges show delamination near the midlength position away from the potted ends. The delamination does not involve all plies. Only one ply interface delaminates in this case. The delamination emanates from the midlength position and extends toward the potted ends. This delamination extends over a longer axial distance than that associated with compressive strength failure, which is discussed later. The positioning of the damage near the

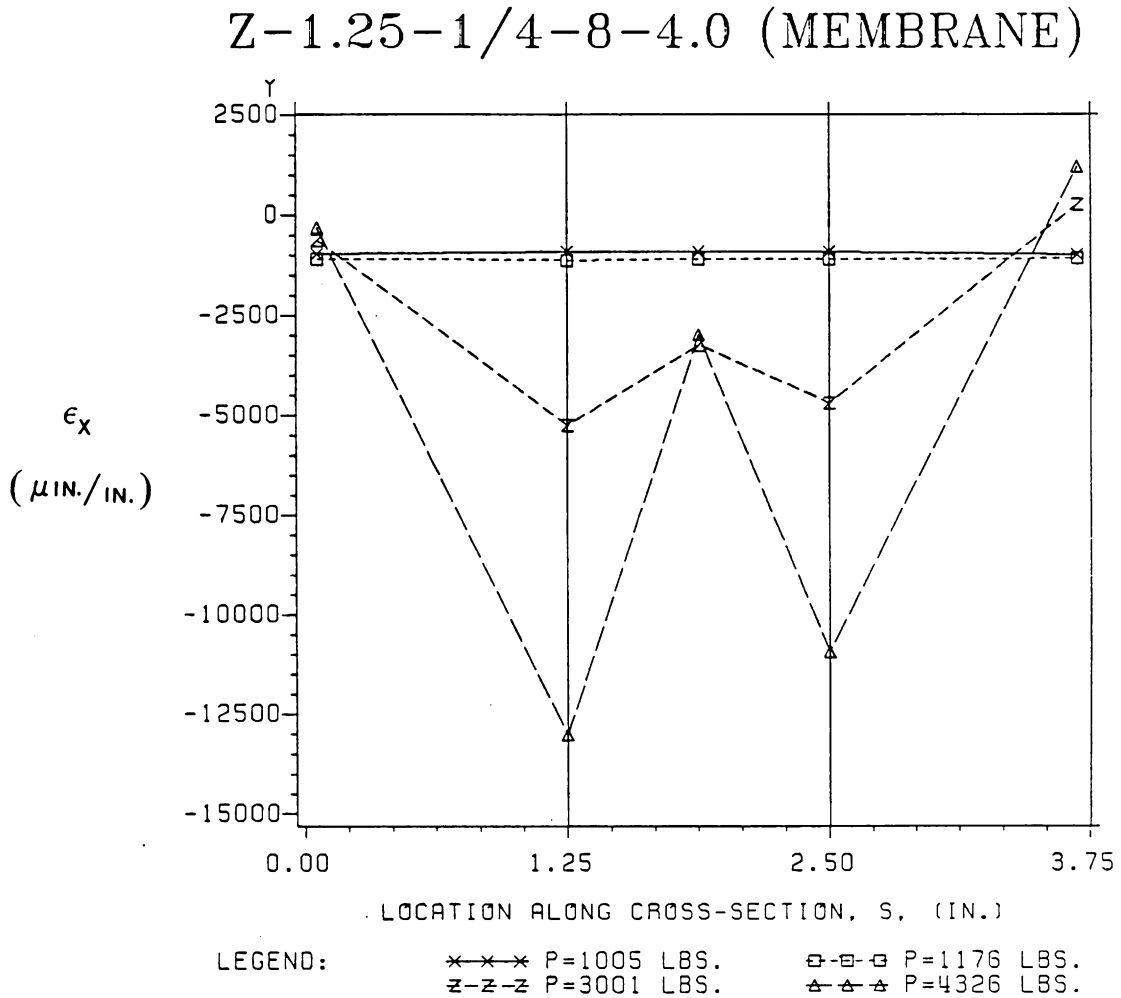

Figure 20: Experimental Membrane Strain Distribution

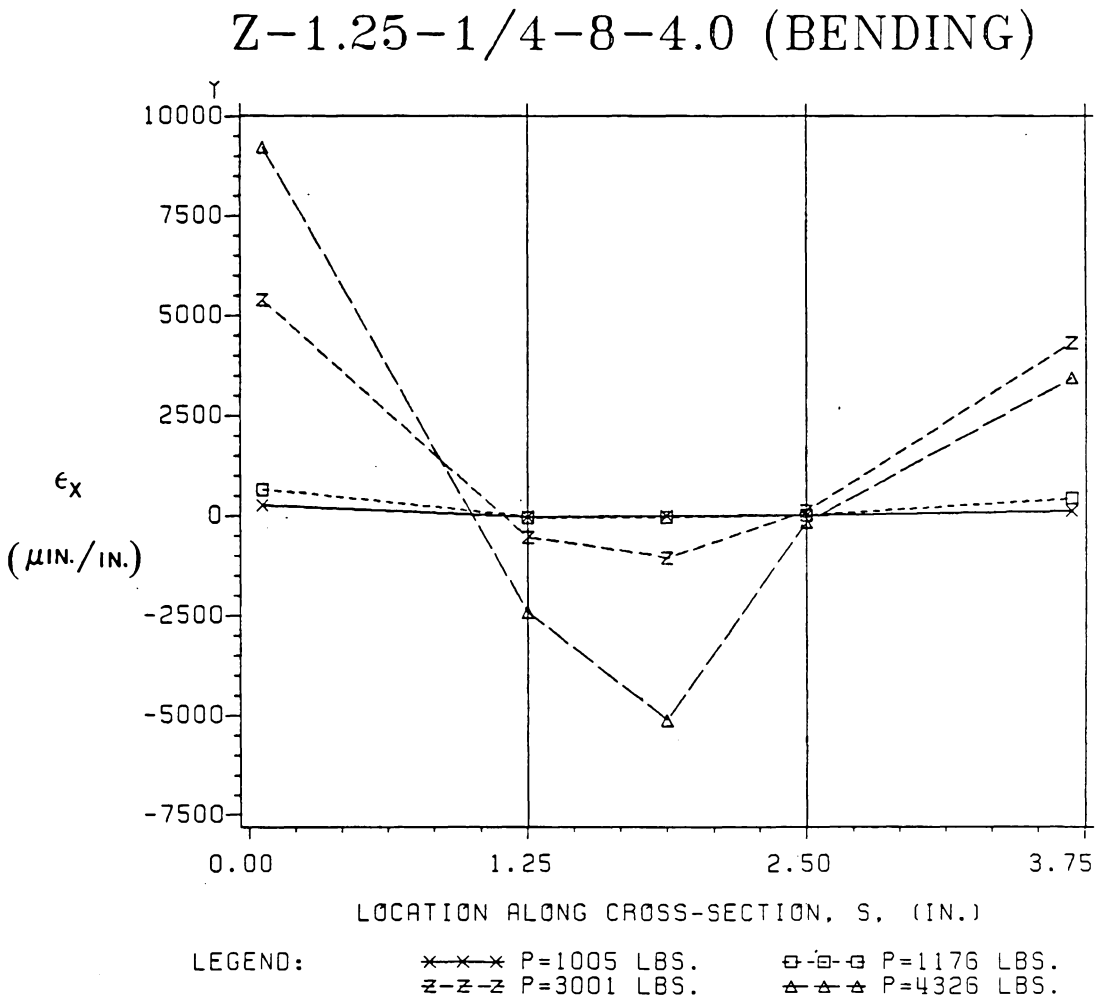

Figure 21: Experimental Bending Strain Distribution

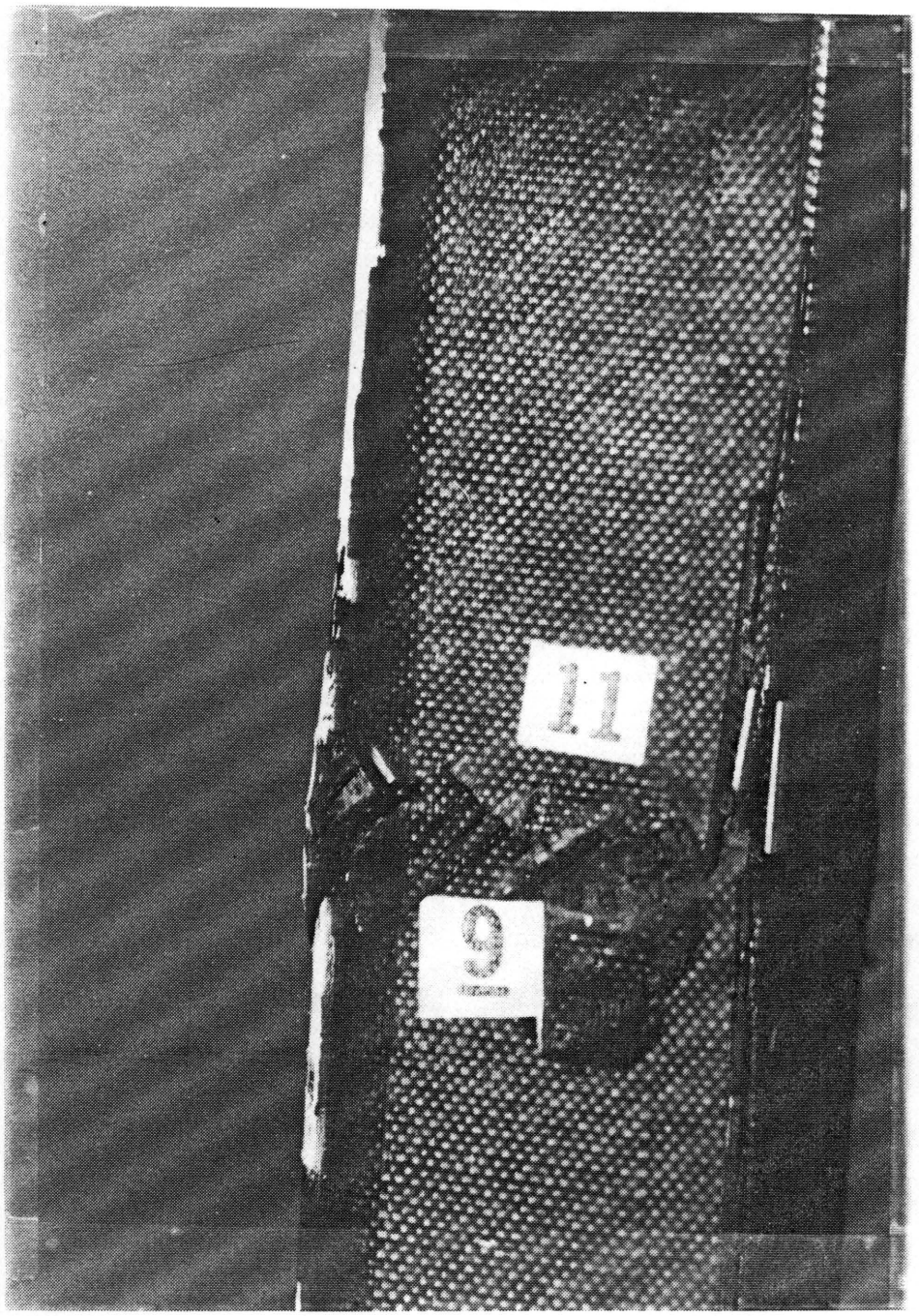

Figure 22: Local Plate Postbuckling Failure -- Edge View

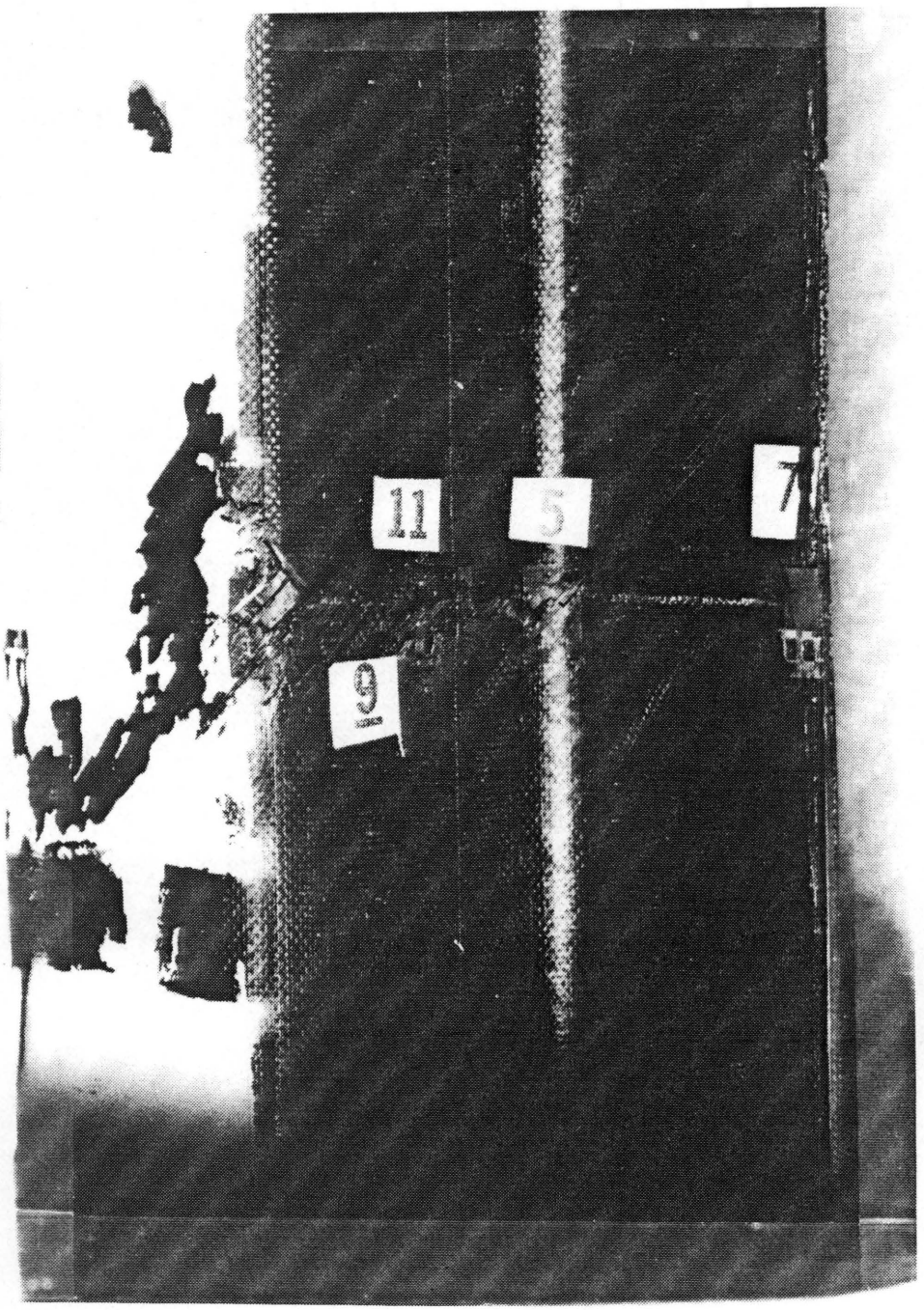

Figure 23: Local Plate Postbuckling Failure -- Oblique View

midlength position is coincident with the buckle wave crest occurring at the midlength position.

Composite stiffener crippling involves significantly different behavior than metal stiffener crippling. Composite stiffener crippling is dominated by corner failure and free edge delamination. In contrast Figure 24 shows a crippled metal channel section where material yielding is the dominant behavior in the crippling mode.

In the past, there has been much work done in the area of metal stiffener crippling. Composite stiffener crippling is a new subject for investigation which requires much more work before it is understood. The data recorded in this study did not supply information as to the relative criticality of corner stresses or free edge stresses to crippling initiation in composites. It did not include internal stress or strain measurements which is what is needed to determine whether corner failure , due to high membrane loads, or free edge delamination, due to high bending loads, is what initiates the crippling process.

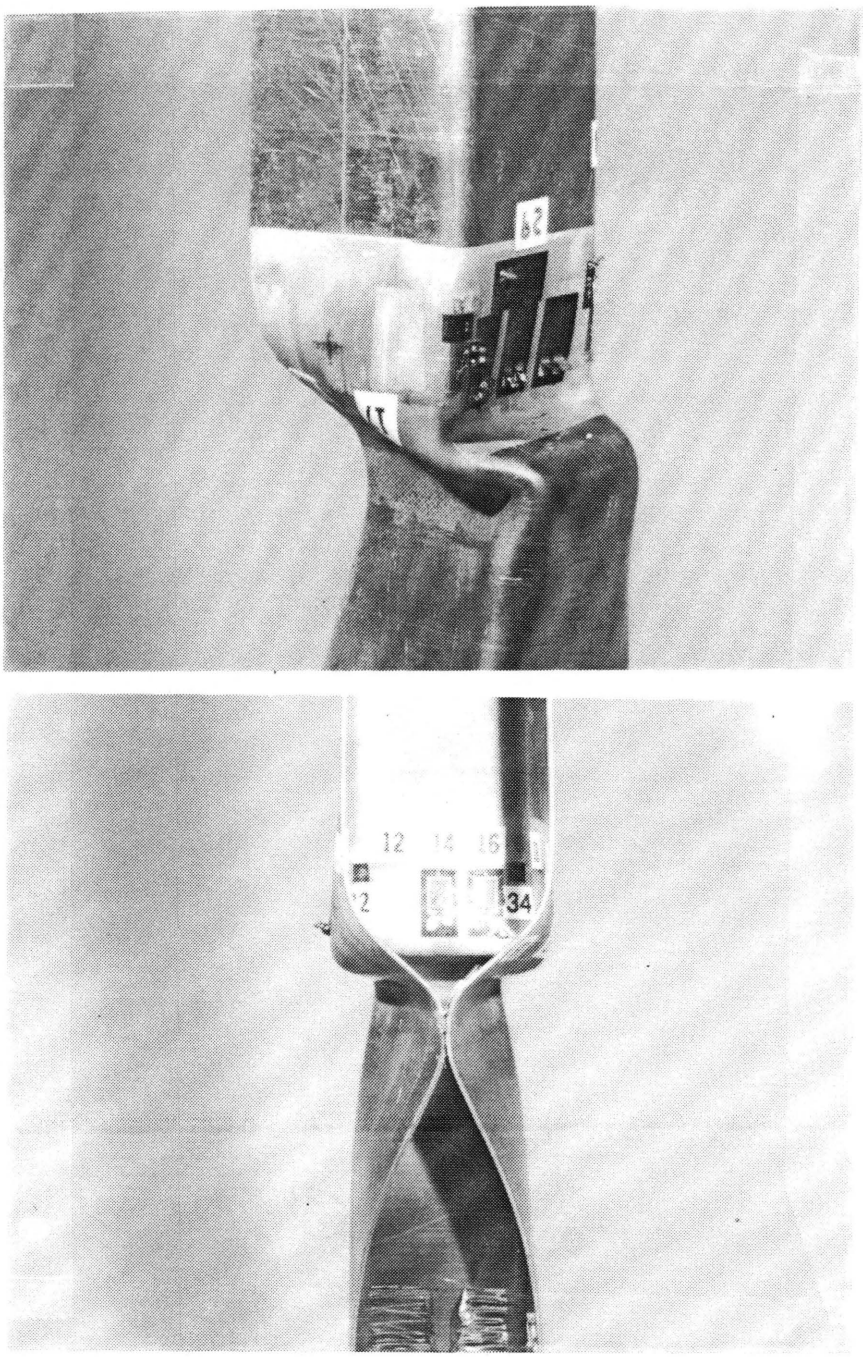

Figure 24: Metal Stiffener Crippling Involving Material Yielding

4.2 GLOBAL COLUMN BUCKLING TO FAILURE

The three channel specimens 2-1, 2-2, and 2-3 in group 2 exhibit column buckling in a combined torsional-flexural mode. Bending occurs about the strong axis. The theoretical membrane strain distribution associated with torsional/strong-axis column buckling can be produced by superimposing a distribution for strong-axis buckling over a distribution for torsional axis buckling.

Brush and Almroth [15] present an analysis for column buckling of open sections. The analysis treats the column buckling problem as an eigenvalue problem with three functional degrees-of-freedom. The degrees-of-freedom are two bending displacements in the directions of the principal axes, and a rotation about the longitudinal torsional axis. The eigenvectors for this problem indicate the relative contributions, of the three degrees-of-freedom, to the buckling mode associated with a particular eigenvalue or buckling load.

For channel cross sections with equal flange widths, the weak-axis degree-of-freedom uncouples from the other two. The minimum eigenvalue is associated with a torsional/strong-axis mode in which the torsional degree-of-freedom dominates (see Figure 25). The eigenvector determines the relative proportions of the two degrees-of-freedom and the

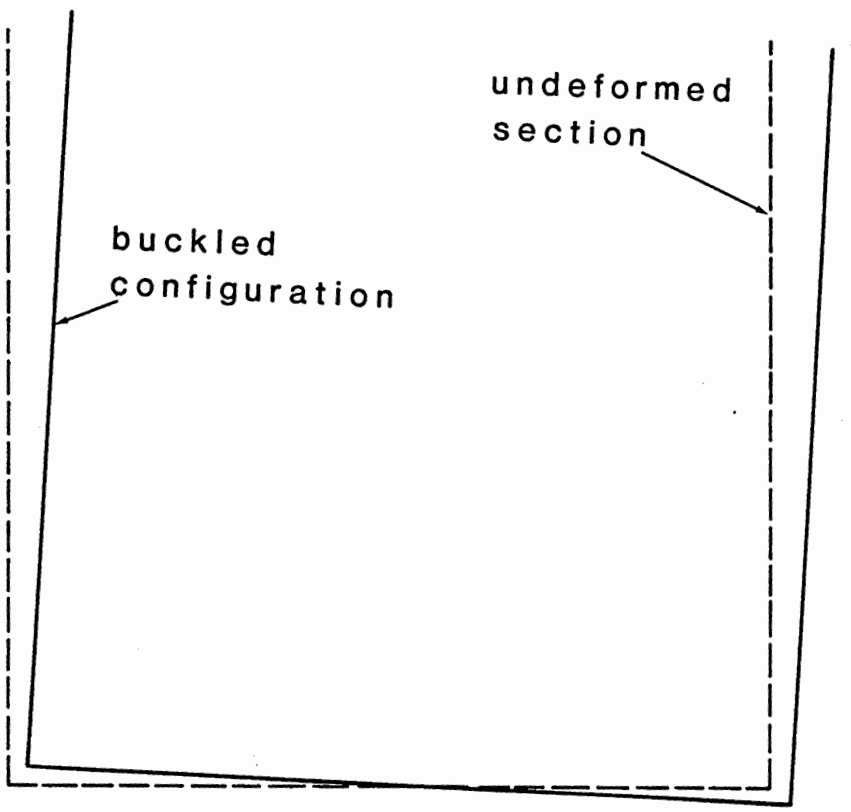

Figure 25: Torsional/Strong-Axis Column Mode

proportions of the associated strain distributions that are combined to give the complete buckling mode shape.

Figure 26 shows the theoretical membrane strain distribution for torsional/strong-axis column buckling. Figure 27 shows the experimental membrane strain distributions for the channel specimen 2-1 in group 2. The development of the theoretical distribution can be found in Appendix B. Note that the theoretical distribution indicates positive strain. This is because it represents the strain distribution due to buckling only and does not include the uniform compressive strain of prebuckling. If a uniform compression strain is added to the distribution shown in Figure 26, it will agree more closely with Figure 27.

The failure of the channels in group 2 was caused by the twisting that dominated the buckling mode. Figures 28 and 29 show specimen 2-1 that actually twisted out of the potting at one end and just started to break at the other end due to twisting.

The zee stiffener 2-4 in group 2 exhibits weak-axis column buckling (see Figure 30). The theoretical membrane strain distribution associated with weak-axis column buckling is shown in Figure 31. The development of this distribution is also given in Appendix B. The experimental membrane strain distribution, for specimen 2-4 at four load

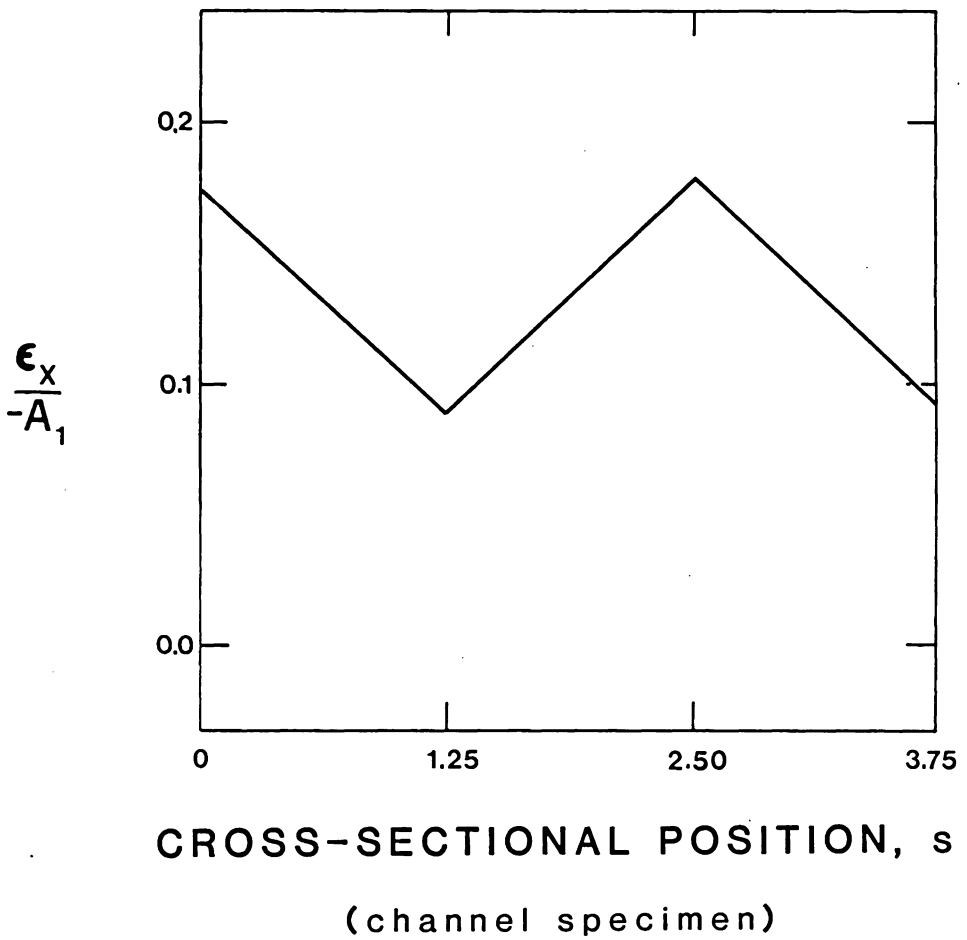

Figure 26: Theoretical Membrane Strain Distribution for the Channel Section at Buckling

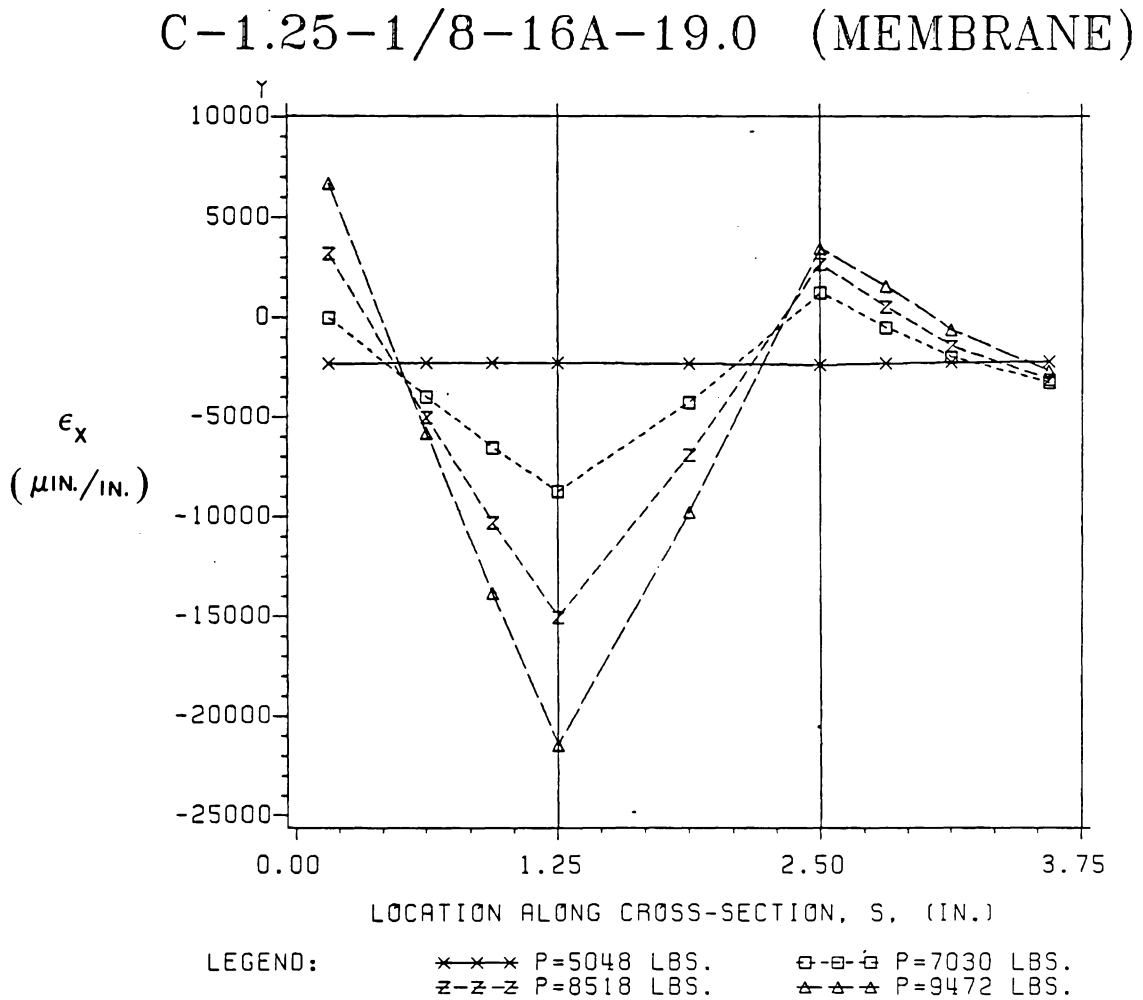

Figure 27: Experimental Membrane Strain Distribution for the Channel Section

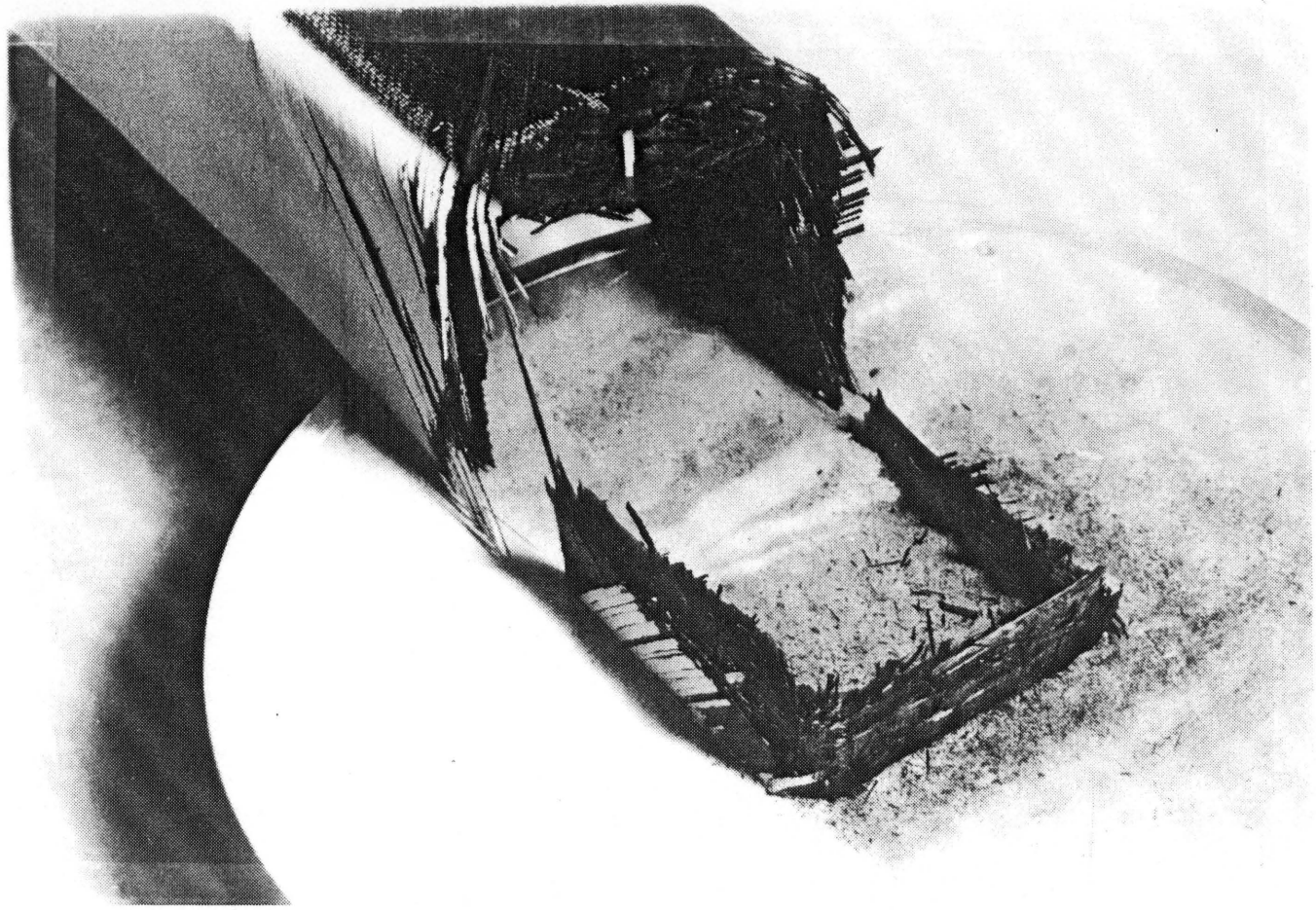

Figure 28: Torsional/Strong-Axis Column Failure -- Broken End

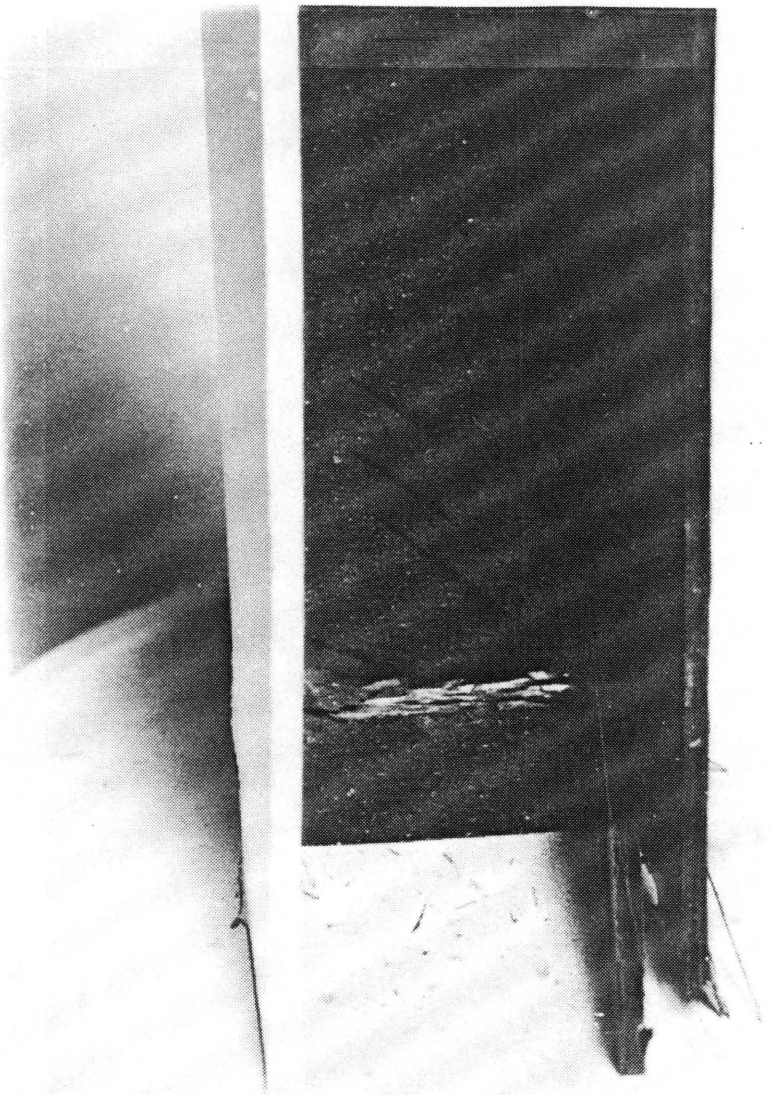

Figure 29: Torsional/Strong-Axis Column Failure -- Cracked End

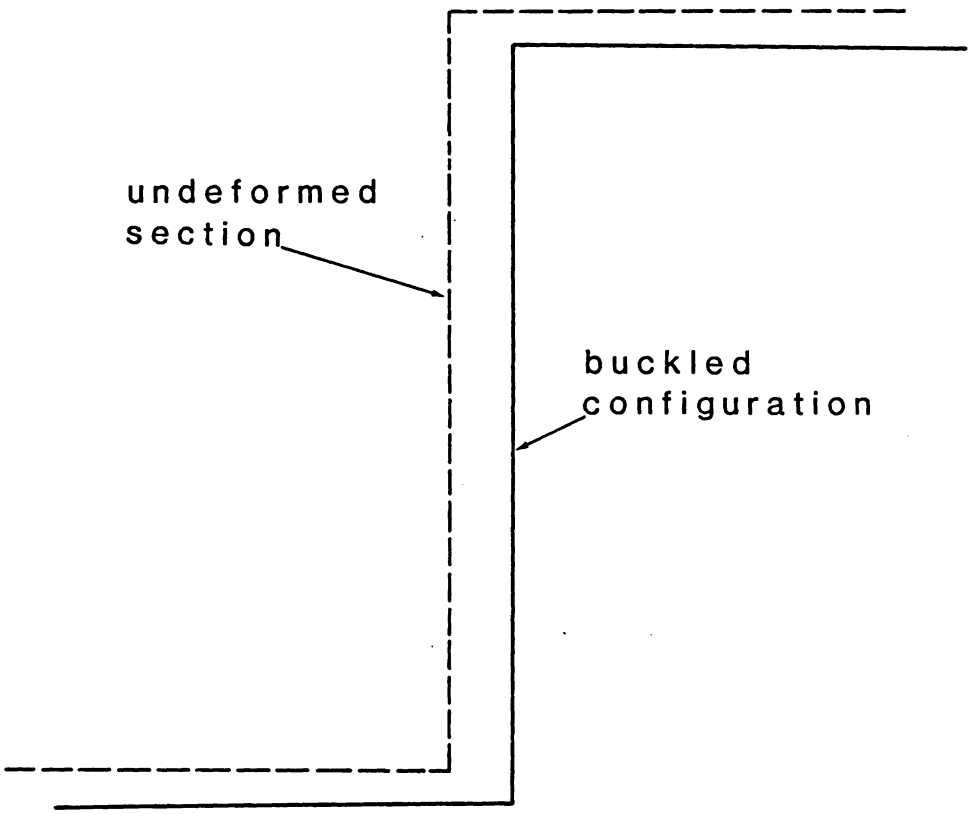

Figure 30: Weak-Axis Column Mode

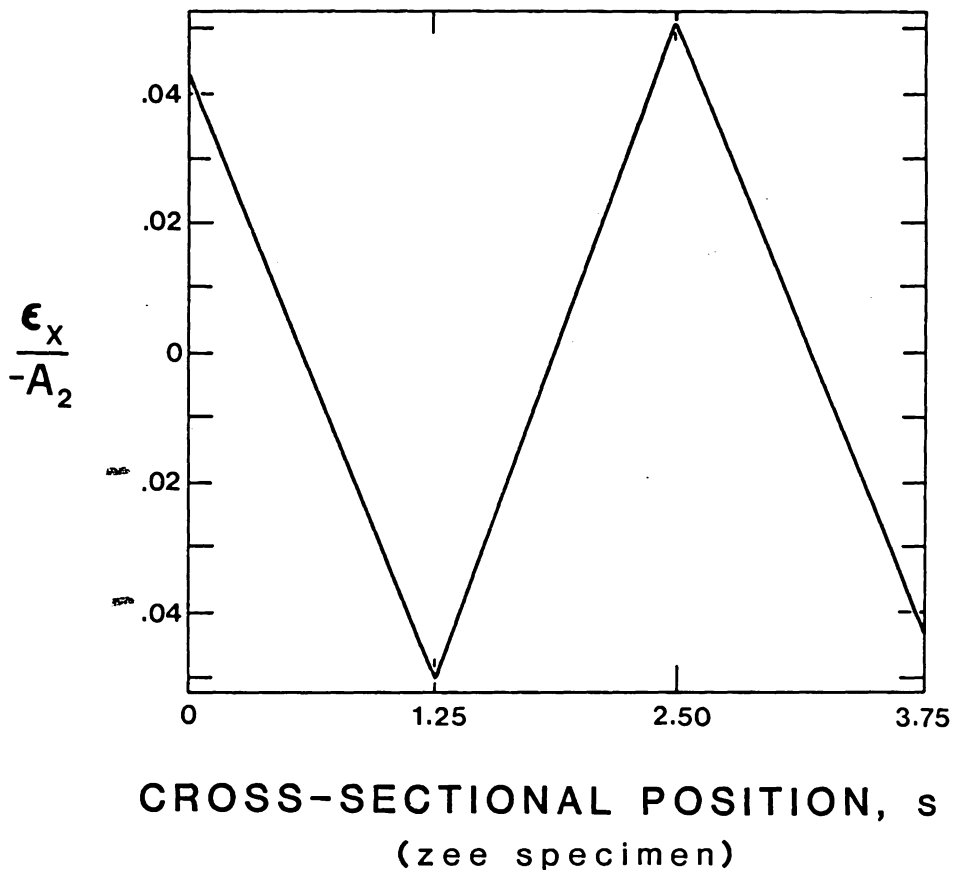

Figure 31: Theoretical Membrane Strain Distribution for the Zee Section at Buckling

levels is shown in Figure 32. The prebuckling strain distributions are uniform as expected. The postbuckling strain distributions show the shape predicted by theory. As discussed before, if a uniform compressive strain distribution is added to the theoretical distribution of Figure 31 it will shift in a negative direction to match more closely the distribution in Figure 32.

Figure 33 shows the potted ends of the failed specimen 2-4 in group 2. The cracks in the potting appear to coincide with the weak axis of the cross section. These cracks indicate that the specimen did buckle around its weak axis. The potting, which restrained the buckling deformation perpendicular to the axis, developed cracks that propagated along the axis.

4.3 SPECIMENS THAT EXHIBIT MATERIAL SHORT COLUMN BEHAVIOR

Group 3 includes one zee specimen, 3-2, and one channel specimen, 3-1 that exhibit very little postbuckling strength. Failure occurred just as the specimen buckled. Since there is practically no postbuckling response the membrane strain distributions should be uniform to failure and the bending strain distributions should be negligible to failure.

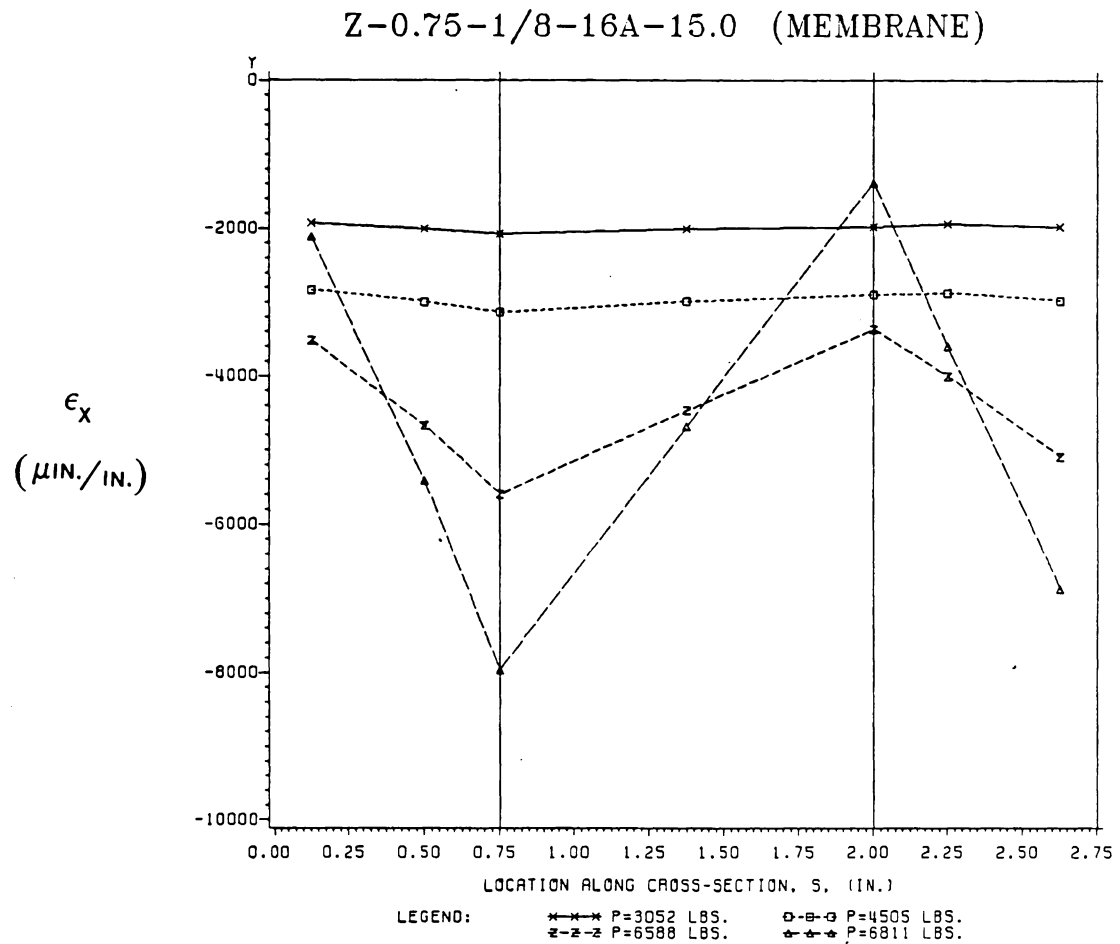

Figure 32: Experimental Membrane Strain Distribution for the Zee Section at Buckling

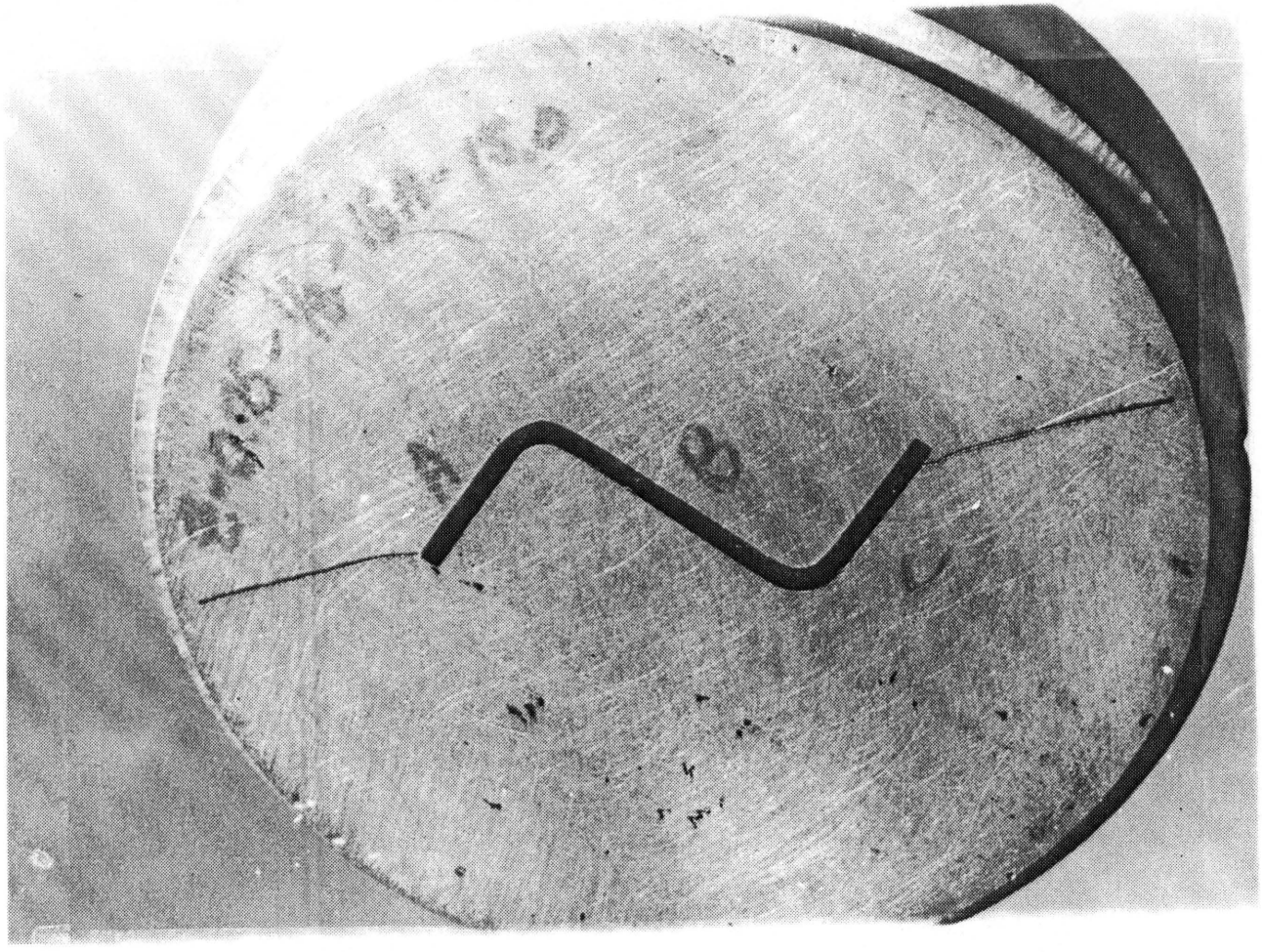

Figure 33: Potting Cracks Along Weak Axis

These observations are supported by the experimental strain distributions of the zee specimen, 3-2,in Figures 34 and 35. Figure 34 shows the nearly uniform membrane distributions at load levels all the way to failure. Figure 35 shows essentially no bending at the first three load levels and some slight bending at failure. The bending strain at failure is an order of magnitude smaller than the membrane strain and could be a result of damage initiation at failure.

Figure 36 shows the failed channel specimen, 3-1, from group 3. The damage is characteristic of compressive failures in laminated composite structures that do not buckle. The behavior of the specimen is understandable since the strain distributions indicate that the specimen carried the applied load without bending.

Delamination associated with compressive strength failure is different from delamination associated with local crippling in group 1. The compressive strength delamination is more complete in the sense that all plies of the laminate, instead of just two, are involved. Another contrast is that the compressive strength delamination does not extend for as long an axial distance as the crippling delamination.

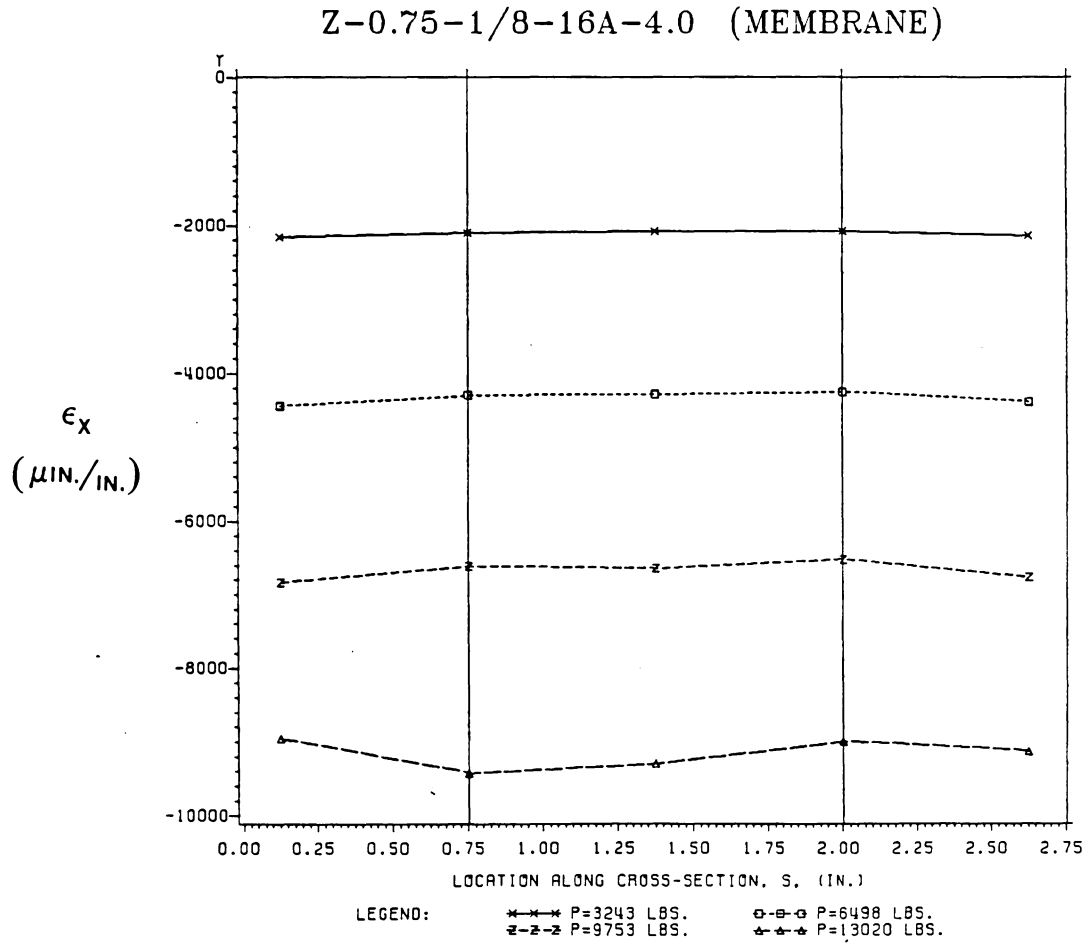

Figure 34: Experimental Membrane Strain Distribution -- Group 3

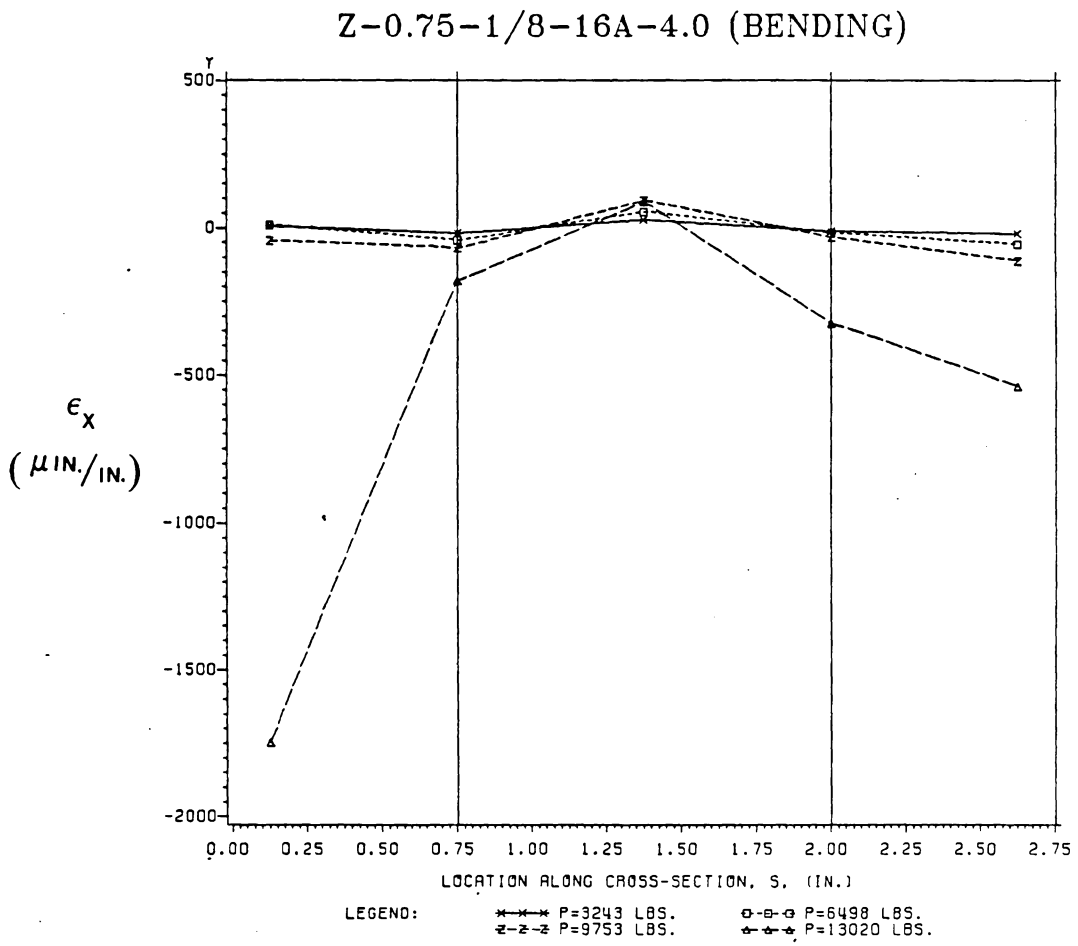

Figure 35: Experimental Bending Strain Distribution -- Group 3

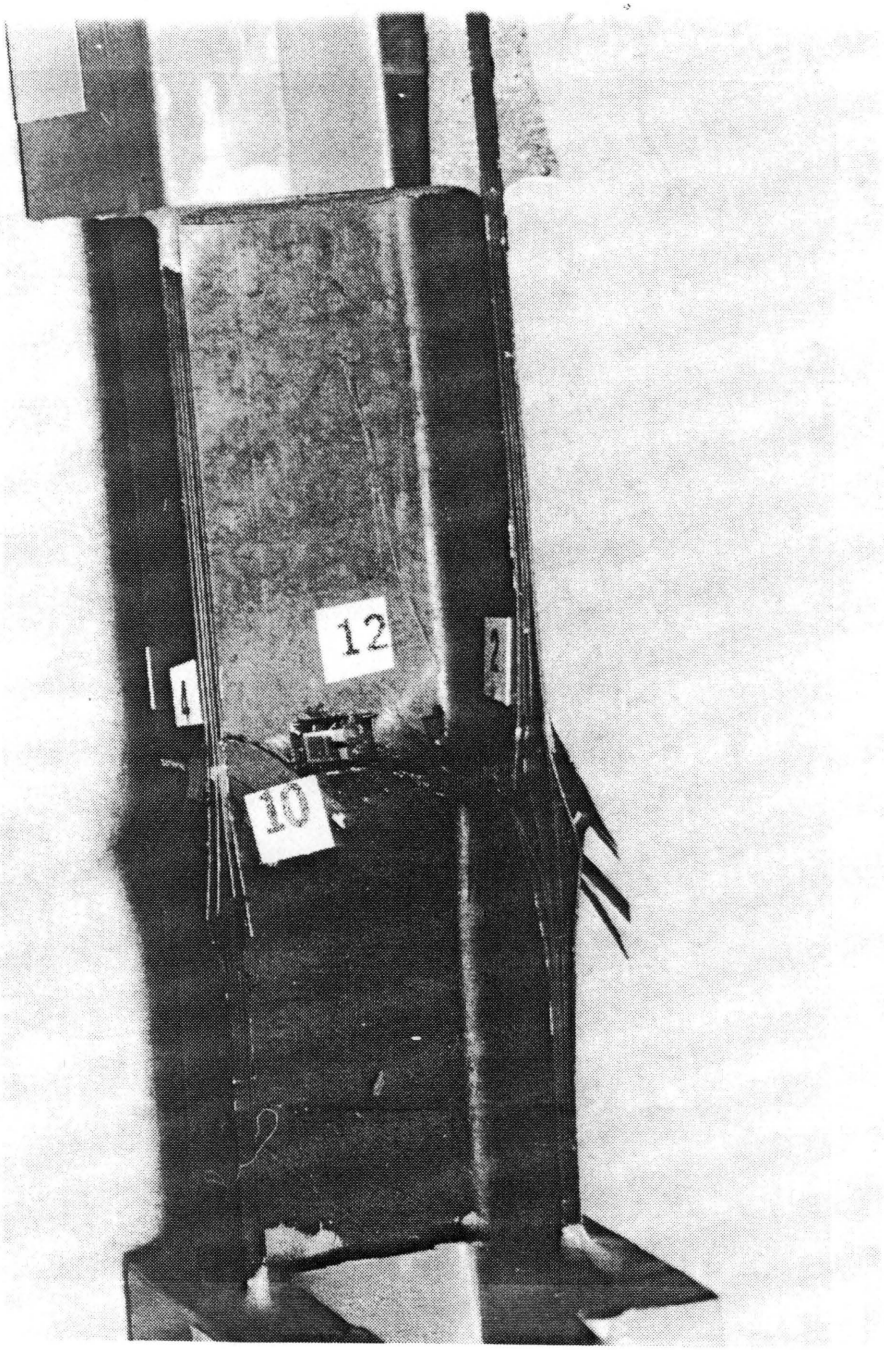

Figure 36: Compressive Strength Failure

4.4 INSTABILITY DUE TO MULTI-MODE DEFORMATION

As discussed earlier, the zee specimen in this group exhibited unstable postbuckling behavior because the flange with its free edge on the compressive side of the weak axis buckled in a plate mode after the entire specimen buckled as a column about the weak axis. This behavior is confirmed by the experimental strain distributions for specimen 4-1 in Figures 37 and 38. The membrane strain distribution (Figure 37) shows the characteristic pattern associated with weak-axis column buckling of zee specimens. The pattern occurs for all but the first load level which corresponds to pre-buckling. The free edge on the compressive side of the weak axis, as shown in Figure 37, corresponds to the right-hand end of the distribution. In Figure 38, the magnitude of the bending strains are small compared to membrane strains shown in Figure 37, except at the compressive free edge position for the highest load level. This confirms that local buckling of that flange occurred after global column buckling of the entire specimen occurred.

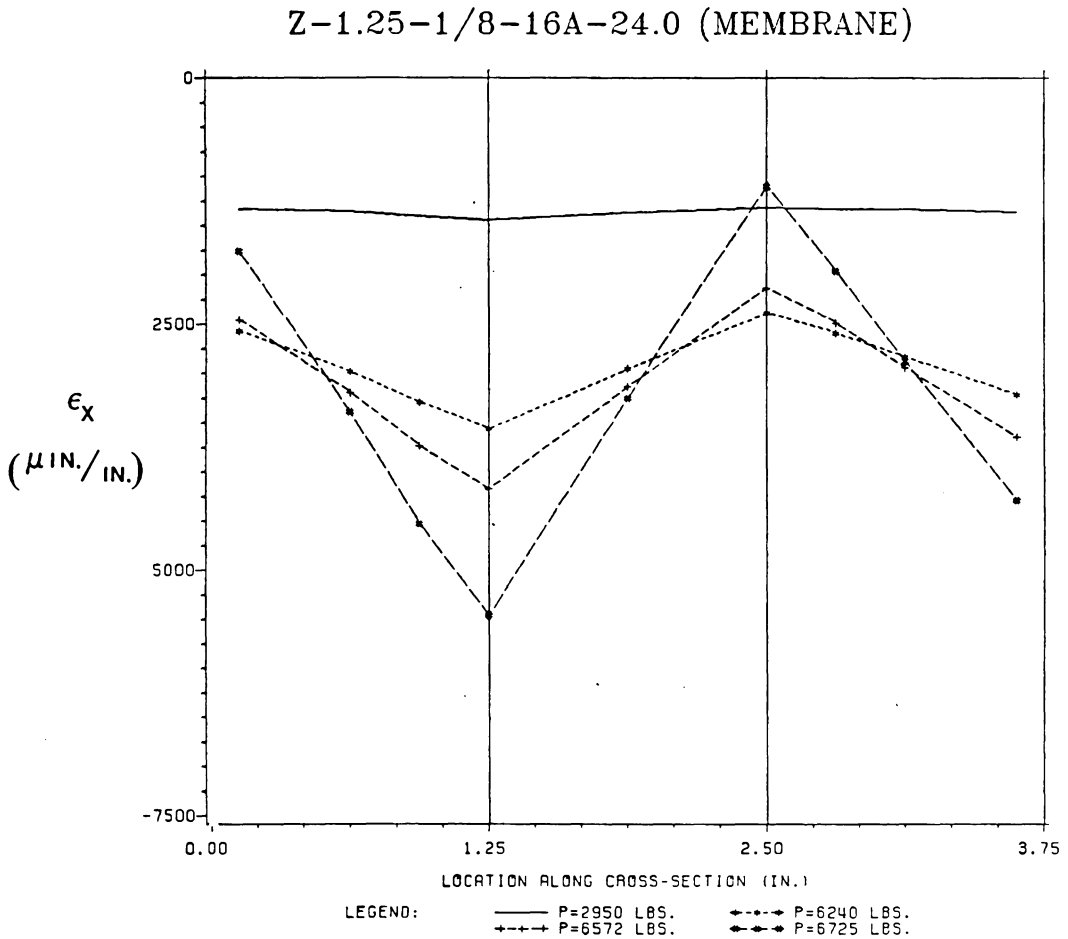

Figure 37: Experimental Membrane Strain Distribution -- Group 4

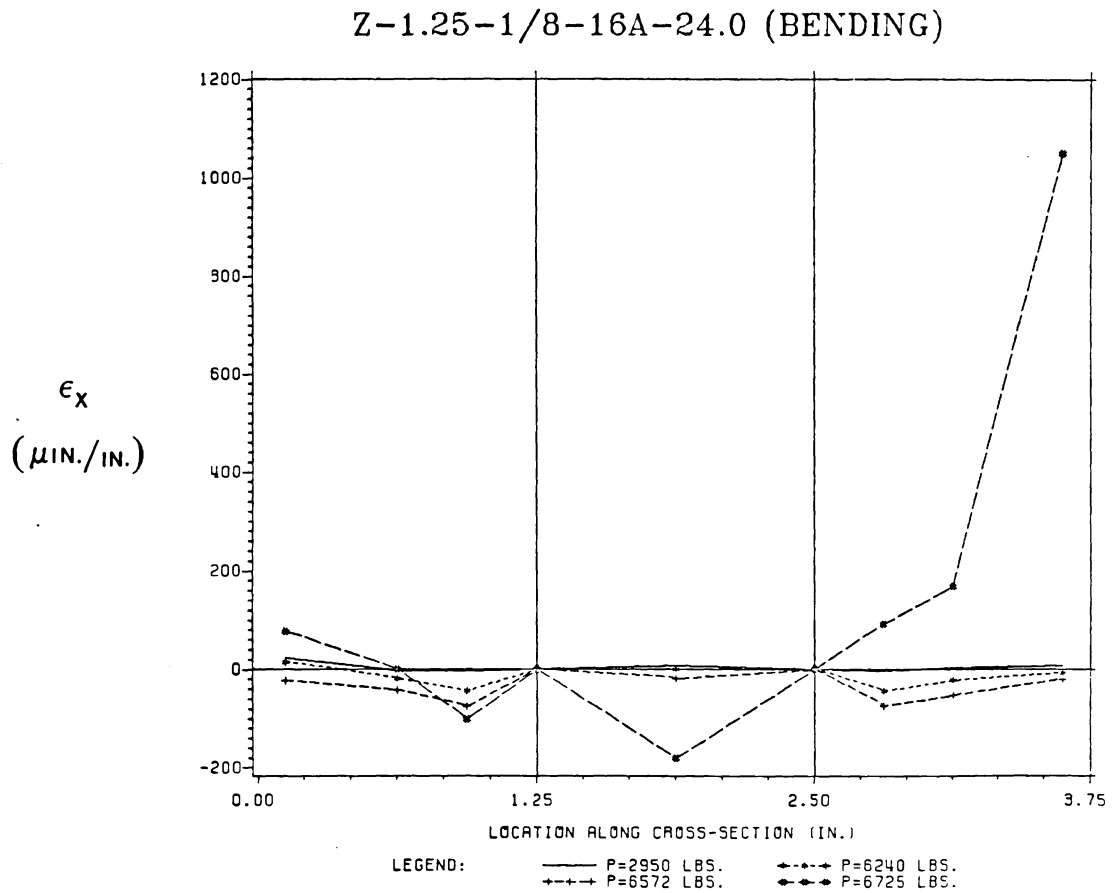

Figure 38: Experimental Bending Strain Distribution -- Group 4

4.5 STRAINS ACROSS THE CROSS SECTION AT FAILURE

Tables 6, 7, and 8 show the axial membrane strains and bending strains at the corners and free edges of the mid-length cross section for each specimen at its failure load. The membrane strain data is presented in rows labeled (M). The bending strain data is presented in rows labeled (B). No conclusions have been drawn from the information. It is presented in order to provide a data base for future work.

It should be noted that corner positions where the bending strain is not reported are positions where inside corner gages were not mounted. The values reported for membrane strain at these locations are the total strain measurements of the outer corner surface.

TABLE 6

Corner and Free Edge Strains at Failure Loads

SPECIMEN NO.	$P_{FAILURE}$ (lbs)	FREE EDGE (μin/in)	CORNER (μin/in)	CORNER (μin/in)	FREE EDGE (μin/in)
1-1 (M)	2805	99	-2404*	-1513*	36
(B)		1906	---	---	1887
1-2 (M)	3091	-58	-3769*	-3154*	-1738
(B)		3587	---	---	464
1-3 (M)	4239	-534	-10200*	-9086*	-307
(B)		6813	---	1295	-3644
1-4 (M)	3947	410	-6941	-8393	420
(B)		-3155	1009	2379	3918
1-5 (M)	4247	-16	-10409	-11048	-298
(B)		6190	186	-2089	9358
1-6 (M)	2903	-535	-13076*	-9144*	818
(B)		-8657	---	---	-2493
1-7 (M)	12426	-3419	-7452*	-7778*	-3200
(B)		10472	---	---	-11745
1-8 (M)	13284	-1149	-6956*	-6746*	-1154
(B)		-11559	---	---	-12320
1-9 (M)	2627	-1654	-6580*	-4288*	-1377
(B)		-5757	---	---	-4373

*Total strain at outside corner location

TABLE 7

Corner and Free Edge Strains at Failure Loads

SPECIMEN NO.	$P_{FAILURE}$ (lbs)	FREE EDGE (μin/in)	CORNER (μin/in)	CORNER (μin/in)	FREE EDGE (μin/in)
1-10 (M)	2754	-32	-2814*	-2186*	-507
(B)		-2683	---	---	-3618
1-11 (M)	3226	-108	-4167	-6459	-1283
(B)		1149	-260	494	-8552
1-12 (M)	3685	162	-6370	-2098	284
(B)		4325	1734	3007	-2728
1-13 (M)	4326	-307	-13026	-10940	1205
(B)		9220	-2415	-171	3440
1-14 (M)	3076	-1007	-5820*	-13230*	-198
(B)		9835	---	---	7934
1-15 (M)	12121	-2420	-8276	-7422	-2390
(B)		-10747	-58	-97	-10249
1-16 (M)	10675	-2307	-3783	-5664	-1835
(B)		6922	448	505	7151
1-17 (M)	2367	-2442	-1635*	-4311*	-1815
(B)		-921	---	---	1134

*Total strain at outside corner location

TABLE 8

Corner and Free Edge Strains at Failure Loads

SPECIMEN NO.	$P_{FAILURE}$ (lbs)	FREE EDGE (μin/in)	CORNER (μin/in)	CORNER (μin/in)	FREE EDGE (μin/in)
2-1 (M)	9472	6656	-21488*	3417*	-2714
(B)		-965	---	---	6155
2-2 (M)	7920	-107	-6743*	-242*	-2822
(B)		-860	---	---	-4111
2-3 (M)	9808	-6842	-6040*	-6636*	-6709
(B)		242	---	---	488
2-4 (M)	6811	-2108	-7964*	-1378*	-6877
(B)		-314	---	---	-573
3-1 (M)	13606	-9843	-9027*	-9043*	-9517
(B)		-2700	---	---	1600
3-2 (M)	13020	-8963	-9422	-9003	-9131
(B)		-1748	-181	-325	-540
4-1 (M)	6725	-1758	-5461*	-1096*	-4285
(B)		77	---	---	1051

*Total strain at outside corner location

Chapter V

SUMMARY AND CONCLUSIONS

5.1 SUMMARY

In this study the failure and crippling of thin-walled open section prismatic compression members was investigated. Twenty-four specimens were tested, 13 of which were channel sections and the other 11 were zee sections. Two of the channel specimens and one of the zee specimens were made of 2024-T3 aluminum. The remaining 21 specimens were made of AS4-3502 graphite-epoxy unidirectional tape. Channel and zee cross sections were chosen because they are commonly used as stiffeners in aircraft structures.

All specimens were tested to failure. Data was recorded with strain gages and direct current displacement transducers (DCDTs). Moire interferometry was used to visualize the buckle pattern of one flange of each specimen during testing.

For each specimen, a theoretical buckling load was calculated and compared to the experimental buckling load. The experimental prebuckling strain data was then used to adjust the fiber direction modulus E_1 (or E in the metal cases). The adjusted value of E_1 was then used to recalculate a new theoretical buckling load.

Based on its experimental response to compressive loading, each specimen was assigned to one of four behavioral groups. The behavioral groups are:

1. Local plate buckling to failure (Crippling)
2. Global column buckling
3. Material short column failure
4. Instability due to multi-mode deformation

The buckling response of each group was confirmed with experimental strain distributions. The experimental distributions were explained by either comparing them qualitatively with theoretical distributions, or in terms of bending or lack of bending of plate elements in the cross section. Investigations of failed specimens were made which showed evidence of the behaviors confirmed by the strain distributions. The experimental observations and data from this study led to the conclusions presented in the following section.

5.2 CONCLUSIONS

The conclusions from this study are presented here for all four behavioral groups.

5.2.1 Group 1 -- Local plate buckling to failure (crippling)

1. The buckling load adjustment procedure succeeded in all but four of the 17 cases. No explanation has been made for the four discrepancies.
2. Experimental axial strain distributions were explained and were indicative of local plate buckling.
3. The crippling failure mode involved cracking of the cross section, especially in the corners, and free edge delamination.
4. The surface strain data did not supply information as to whether crippling initiated in the corners or at the free edge of the cross section.
5. The delamination associated with crippling did not involve all plies of the laminate and extended over a relatively long axial distance compared to the delamination associated with compressive strength failure.

5.2.2 Group 2 -- Global column buckling

1. The buckling load adjustment did not succeed in any of the four cases in group 2. This was attributed to end fixity uncertainty of the potting material.

2. The end fixity was less than clamped and led to unexpected column buckling behavior of specimens that were assumed to be clamped and were predicted to exhibit local plate buckling behavior.
3. The experimental membrane strain distributions for this group were explained and were indicative of the column buckling modes associated with channels (torsional/strong-axis) and zees (weak-axis).
4. The column behaviors were confirmed by photographs that showed evidence of torsional/strong-axis buckling of the channels and weak-axis buckling of the zees.

5.2.3 Group 3 -- Material Short Column Failure

1. The buckling load adjustment procedure was successful for both cases.
2. Experimental axial strain distributions were explained and were indicative of the lack of bending associated with the response of these specimens.
3. The lack of bending was confirmed by photographs of the failed specimen that showed the characteristics of compressive strength failure of laminated composites that do not buckle.

4. In contrast to the delamination associated with crippling, the delamination associated with compressive strength failure involved all plies of the laminate and extended over a relatively short axial distance.

5.2.4 Group 4 -- Instability due to multi-mode deformation

1. The instability was attributed to an additional mode of deformation, local plate buckling, that softened the structure after weak-axis column buckling had occurred.
2. Experimental axial strain distributions confirmed this multi-mode behavior.

5.3 SUGGESTIONS FOR FUTURE WORK

More work needs to be done to develop a failure analysis for stiffener crippling that includes corner cracking and free edge delamination as basic failure modes. This analysis should determine the criticality of free edge delamination and damage of the stiff corner region in stiffener crippling. In order to establish the criticality of free edge delamination vs. corner failure it is suggested that both an experimental and theoretical approach be considered.

One possible experimental approach is to test specimens with and without capped free edges. If the capping

increased the crippling load significantly, then free edge delamination (delayed by capping) would be more critical than corner failure. If the crippling load did not increase with capping, corner failure would be more critical than free edge delamination.

In addition to testing, nonlinear postbuckling analyses need to be performed to determine internal stress distributions of the cross section. The distribution could supply information about the relative probability of free edge delamination and corner failure in the cross section.

Work also needs to be done in the area of torsional instability of laminated composite structures. In this report, an isotropic formulation was used to develop a theoretical strain distribution to compare to experimental strain distributions obtained from graphite-epoxy structures. This served as a satisfactory qualitative comparison method and was all that was needed. In general, a more detailed formulation is needed that takes into account the orthotropy of graphite-epoxy material systems.

REFERENCES

1. Lundquist, E. E., and Schuette, E. H., "Critical Stresses for Plates", NACA ARR No. 3J27, 1943.

2. Stowell, E. Z., Heimerl, G.J., Libove, C., and Lundquist, E. E., "Buckling Stresses for Flat Plates and Sections", ASCE Proceedings, Vol. 77, July 1951.

3. Gerard, G., Introduction to Structural Stability Theory, McGraw-Hill, New York, 1962, pp. 66-70.

4. Schuette, E. H., "Observations of the Maximum Average Stress of Flat Plates Buckled in Edge Compression", NACA TN 1625, 1949.

5. Peery, D. J., Aircraft Structures, McGraw-Hill, New York, 1950, pp. 382-386.

6. Spier, E. E., "On Crippling and Short Column Buckling of Graphite-Epoxy Structures with Arbitrary Symmetrical Laminates",SESA 1977 Spring Meeting, Dallas, TX, May,1977.

7. Spier, E. E., "On Experimental versus Theoretical Incipient Buckling of Narrow Graphite/Epoxy Plates in Compression", AIAA paper 80-0686, 1980.

8. Gerard, G., "Handbook of Structural Stability; Part IV-Failure of Plates and Composite Elements", NACA TN 3784, 1957, pg. 26.

9. Spier, E. E., and Klouman, F. L., "Empirical Crippling Analysis of Graphite/Epoxy Laminated Plates",Composite Materials: Testing and Design (4th Conf.), ASTM STP 617, 1977, pp. 255-271.

10. Stroud, W. J., and Anderson, M. S., "PASCO: Structural Panel Analysis and Sizing Code, Capability and Analytical Foundations", NASA TM-80181, 1980.

11. Wittrick, W. H., and Williams, F. W., Buckling and Vibration of Anisotropic or Isotropic Plate Assemblies Under Combined Loadings, Int. J. Mech. Sci., Vol. 16, 1974.

12. Jackson, D. G., Qualification of Hercules AS4/3502 Graphite/Epoxy Prepreg Tape System to FMS-2023, General Dynamics, Fort Worth, Texas, 1982.

13. Quality Assurance Certification -- Lot No. 2015-2, Hercules Incorporated, Magna, Utah, 1981.

14. Jones, R. M., Mechanics of Composite Materials, McGraw-Hill, New York, 1975, pp. 147-156.

15. Brush, D. O., and Almroth, B. O., Buckling of Bars, Plates, and Shells, McGraw-Hill, New York, 1975, pp. 37-51.

Appendix A

CLAMPED EFFECTIVE LENGTH OF TORSIONAL/STRONG-AXIS COLUMNS

Details of this discussion can be found in Section 2.3 of Brush and Almroth [15]. For a channel section with equal flange widths, the weak axis, the strong axis, the centroid and the shear center are postioned as shown in Figure 17. The column buckling analysis used here involves three functional degrees-of-freedom, ϕ, v, and w. The angle ϕ is the torsional rotation about the longitudinal axis through the shear center, and v and w are bending displacements of the shear center in the direction of the principal axes Y and Z. Assumed displacement fields of the form,

$$\phi = A_1\left(1 - \cos\frac{2\pi x}{L}\right) \qquad v = A_2\left(1 - \cos\frac{2\pi x}{L}\right) \qquad w = A_3\left(1 - \cos\frac{2\pi x}{L}\right)$$

where A_1, A_2, and A_3 are constants, satisfy clamped boundary conditions (ϕ=v=w=ϕ'=v'=w'=0), and are solutions of the governing differential equations

$$\begin{aligned} EI_{yy}w^{iv} + P(w-y_o\phi)'' &= 0 \\ EI_{zz}v^{iv} + P(v+z_o\phi)'' &= 0 \\ EC_w\phi^{iv} - (GJ - \frac{I_o}{A}P)\phi'' - Py_ow'' + Pz_ov'' &= 0 \end{aligned} \qquad \text{(A1)}$$

In these equations, E is Young's modulus, I_{yy} and I_{zz} are the moments of inertia about the Y and Z axes, respectively, y_o and z_o are the coordinates of the shear center with respect to the centroid, C_w is the warping constant, G is the shear modulus, J is the torsional constant, I_o is the polar moment of inertia about the shear center, and A is the cross-sectional area. Substitution of the assumed displacement fields into the differential equations yields three algebraic equations in A_1, A_2, and A_3,

$$\begin{aligned} Pz_oA_1 + (P-P_z)A_2 &= 0 \\ Py_oA_1 - (P-P_y)A_3 &= 0 \\ \frac{I_o}{A}(P - P_\phi)A_1 + Pz_oA_2 - Py_oA_3 &= 0 \end{aligned} \qquad \text{(A2)}$$

where

$$P_\phi = \left(\frac{4\pi^2}{L^2}EC_w + GJ\right)\frac{A}{I_o} \qquad P_y = \frac{4\pi^2 EI_{yy}}{L^2} \qquad P_z = \frac{4\pi^2 EI_{zz}}{L^2}$$

For a channel with equal flange widths, z_o=0. This causes the first equation in (A2) to decouple from the other two. The three eigenvalues then represent, either a pure weak-axis buckling load, P_z (nontrivial solution to the first equation) or two buckling loads associated with coupled torsional and strong-axis buckling modes. The mini-

mum of the three eigenvalues is a torsional/strong-axis buckling load that is the solution of the equation,

$$\frac{I_o}{A}(P - P_\phi)(P - P_y) - (Py_o)^2 = 0 \qquad \text{(A3)}$$

which comes from requiring the determinant of coefficients to vanish in the last two equations of (A2) after setting $z_o = 0$.

For example, consider the case where,

$b_f = b_w = 1.25$ in $E = 10.6 \times 10^6$ psi

$L = 19.0$ in $\nu = 0.3$

$t = .08$ in $G = \frac{E}{2(1+\nu)}$

For this geometry and material, the buckling loads are

$P_1 = 12883$ lbs $P_2 = 334500$ lbs $P_z = 60375$ lbs

The eigenvector associated with the load P_1 =12883 lbs is,

$$\begin{Bmatrix} A_1 \\ A_3 \end{Bmatrix} = \begin{Bmatrix} -7.56 \\ 1 \end{Bmatrix} \qquad \text{(A4}$$

indicating the domination of torsional rotation in the mode.

In this study the effective length factor is defined as

$$\frac{L_{SS}}{L_{CL}} = \text{FACTOR}$$

where $P_{SS}^{CR} = P_{CL}^{CR}$. In the classical case of weak-axis column buckling this factor is equal to 0.5. To determine the effective length factor for this example, the length of a simply supported column of the same cross section and material, with a buckling load of 12883 lbs is required.

For simple support boundary conditions, new solution forms are assumed that satisfy the boundary conditions $\phi=v=w=\phi''=v''=w''=0$. They are,

$$\phi = A_1 \sin\frac{\pi x}{L} \qquad v = A_2 \sin\frac{\pi x}{L} \qquad w = A_3 \sin\frac{\pi x}{L} \quad .$$

Substitution into (A1) gives the same algebraic equations as (A2), but the values of P_ϕ, P_y, P_z change to

$$P_\phi = \left(\frac{\pi^2}{L^2} EC_w + GJ\right) \frac{A}{I_o} \qquad P_y = \frac{\pi^2 EI_{yy}}{L^2} \qquad P_z = \frac{\pi^2 EI_{zz}}{L^2} \quad .$$

The coordinate, z_o is still equal to zero so once again the eigenvalues are separated into P_z, and P_1 and P_2 where P_1 and P_2 are solutions of equation (A3).

Since the same system of equations is solved to determine P_z , P_1, and P_2, the same eigenvalues will be obtained if P_ϕ, P_y, and P_z for the simply supported case are identical to those for the clamped case. Investigation of the expressions for P_ϕ, P_y, and P_z for simply supported boundary conditions indicates that every term in which the quantity $\frac{\pi^2}{L^2}$ appears is multiplied by a factor of 1. The corresponding

terms for clamped boundary conditions are multiplied by a factor of 4. Since these terms are the only places where column length, L, appears, the quantities P_ϕ, P_y, and P_z can be made equal by setting the simply supported length equal to 1/2 the clamped length, thus making the eigenvalues identical for both clamped and simply supported boundary conditions.

This example shows that for the more complicated mode of combined torsional/strong-axis buckling, the effective length factor that relates clamped and simply supported boundary conditions is

$$\frac{L_{SS}}{L_{CL}} = 0.5$$

just as it is for classical weak-axis buckling.

Appendix B

DEVELOPMENT OF GLOBAL COLUMN BUCKLING STRAIN DISTRIBUTIONS

Details of the discussion presented here can be found in Section 2.3 of Brush and Almroth [15]. For channel and zee sections, the weak and strong axes, the centroid and shear center are oriented as shown in Figure 17. The degrees-of-freedom for this column buckling analysis are ϕ, v, and w. The angle ϕ is the rotation about the torsional axis (through the shear center S), and v and w are bending displacements of the shear center along the Y and Z axes respectively. Assumed displacement fields of the form,

$$\phi = A_1(1 - \cos\frac{2\pi x}{L}) \qquad v = A_2(1 - \cos\frac{2\pi x}{L}) \qquad w = A_3(1 - \cos\frac{2\pi x}{L})$$

where A_1, A_2, and A_3 are constants, satisfy clamped boundary conditions (ϕ=v=w=ϕ'=v'=w'=0) and are solutions of the governing differential equations.

$$\begin{aligned} EI_{yy}w^{iv} + P(w-y_o\phi)'' &= 0 \\ EI_{zz}v^{iv} + P(v+z_o\phi)'' &= 0 \\ EC_w\phi^{iv} - (GJ - \frac{I_o}{A}P)\phi'' - Py_ow'' + Pz_ov'' &= 0 \end{aligned} \tag{B1}$$

In these equations, E is Young's modulus, I_{yy} and I_{zz} are the moments of inertia about the Y and Z axes respectively, y_o, and z_o, are the coordinates of the shear center with respect to the centroid, C_w is the warping constant, G is the shear modulus, J is the torsional constant, I_o is the polar moment of inertia about the shear center, and A is the cross-sectional area. Substitution of the assumed displacement fields into the differential equations yields three algebraic equations in A_1, A_2, and A_3. They are,

$$\begin{aligned} Pz_oA_1 + (P-P_z)A_2 &= 0 \\ Py_oA_1 - (P-P_y)A_3 &= 0 \\ \frac{I_o}{A}(P-P_\phi)A_1 + Pz_oA_2 - Py_oA_3 &= 0 \end{aligned} \qquad \text{(B2)}$$

where

$$P_\phi = \left(\frac{4\pi^2}{L^2}EC_w + GJ\right)\frac{A}{I_o} \qquad P_y = \frac{4\pi^2 EI_{yy}}{L^2} \qquad P_z = \frac{4\pi^2 EI_{zz}}{L^2} .$$

For the case of a zee stiffener the centroid and the shear center coincide and $y_o = z_o = 0$. This condition decouples equations (B2) making P_ϕ, P_y, and P_z the three eigenvalues of the system. The lowest value is P_z which corresponds to weak-axis buckling. The strain distribution caused by bending around the weak axis is of the form

$$\varepsilon_x = y\kappa \qquad , \qquad \text{(B3)}$$

where

$$\kappa = v_{,xx} = A_2\left(\frac{2\pi}{L}\right)^2 \cos\frac{2\pi x}{L} \qquad \text{(B4)}$$

At the midlength position (x=L/2),

$$\kappa = - A_2\left(\frac{2\pi}{L}\right)^2 \qquad \text{(B5)}$$

A strain distribution across the cross section is obtained by determining the value of $y\kappa$ across the cross section. In Figure 17 y varies in a piecewise linear manner with respect to the cross-sectional position, s. This variation is given by

$$\begin{aligned}
y &= (b_f - s)\cos\theta - \frac{b_w}{2}\sin\theta \; ; && 0 \leq s \leq b_f \\
y &= \left(s - b_f - \frac{b_w}{2}\right)\sin\theta \; ; && b_f \leq s \leq b_f + b_w \\
y &= (b_f + b_w - s)\cos\theta + \frac{b_w}{2}\sin\theta \; ; && b_f + b_w \leq s \leq 2b_f + b_w
\end{aligned} \qquad \text{(B6)}$$

For example, when

$$b_f = b_w = 1.25 \text{ in} \qquad L = 19.0 \text{ in}$$

then

$$\theta = 47.3°$$

where θ is defined in Figure 17. The strain distribution is given by

$$\varepsilon_x = -.1094\ A_2 \left[(b_f - s)\cos\theta - \frac{b_w}{2}\sin\theta\right] ;\quad 0 \leq s \leq b_f$$

$$\varepsilon_x = -.1094\ A_2 \left[(s - b_f - \frac{b_w}{2})\sin\theta\right] ;\quad b_f \leq s \leq b_f + b_w \qquad \text{(B7)}$$

$$\varepsilon_x = -.1094\ A_2 \left[(b_f + b_w - s)\cos\theta + \frac{b_w}{2}\sin\theta\right] ;\quad b_f + b_w \leq s \leq 2b_f + b_w$$

Substituting the above values for b_f, b_w, and θ into equation (B7) gives

$$\varepsilon_x = -A_2\ (.04249 - .07420\ s) ;\quad 0 \leq s \leq b_f$$

$$\varepsilon_x = -A_2\ (.08040\ s - .1507) ;\quad b_f \leq s \leq b_f + b_w \qquad \text{(B8)}$$

$$\varepsilon_x = -A_2\ (.2357 - .07420\ s) ;\quad b_f + b_w \leq s \leq 2b_f + b_w$$

Evaluating ε_x at s=0, b_f, b_f+b_w, and $2b_f+b_w$ gives

s	$\varepsilon_x/-A_2$
0	.04299
1.25	-.05026
2.50	.05030
3.75	-.04255

A plot of $\frac{\varepsilon_x}{-A_2}$ vs. cross-sectional position, s, is shown in Figure 31. This distribution is due to bending only (i.e. the $y\kappa$ term). The total strain distribution also includes a constant uniform compression term (ε^o) that shifts the

entire bending distribution uniformly in the negative direction.

In the case of a channel stiffener, the centroid and shear center are not coincident. They are aligned along the strong axis of the cross section such that $z_o = 0$ and $y_o \neq 0$. This condition decouples the first equation of (B2) from the other two. The three eigenvalues then, represent either a pure weak-axis buckling load, P_z,(solution to the first equation) or two buckling loads that are associated with coupled torsional/strong-axis buckling. To determine the theoretical strain distribution for combined torsional/strong-axis buckling a specific example is used. Consider a channel where,

$$b_w = b_f = 1.25 \text{ in}$$
$$t = .08 \text{ in}$$
$$L = 19.0 \text{ in}$$
$$E = 10.6 \times 10^6 \text{ psi}$$
$$\nu = 0.3$$
$$G = \frac{E}{2(1+\nu)}$$

For this configuration and material the three buckling eigenvalues are

$$P_z = 60375 \text{ lbs} \qquad P_1 = 12883 \text{ lbs} \qquad P_2 = 334500 \text{ lbs}$$

where P_z is the weak-axis buckling load and P_1 and P_2 are the combined torsional/strong-axis buckling loads. The eigenvector associated with the minimum eigenvalue, P_1, is

$$\begin{Bmatrix} A_1 \\ A_3 \end{Bmatrix} = \begin{Bmatrix} -7.56 \\ 1 \end{Bmatrix} \tag{B9}$$

which indicates that the twisting rotation, ϕ, dominates the mode associated with the load, P_1.

Since the buckling mode of interest consists of a torsional and a strong-axis component, the cross-sectional strain distribution is developed by superimposing a strong-axis buckling strain distribution on a torsional axis buckling strain distribution in the proportions dictated by the eigenvector in equation (B9). The cross-sectional strain distribution caused by strong-axis bending is

$$\varepsilon_x = z\kappa \quad , \tag{B10}$$

where

$$\kappa = w_{,xx} = A_3\left(\frac{2\pi}{L}\right)^2 \cos\frac{2\pi x}{L} \quad . \tag{B11}$$

At the midlength position (x=L/2),

$$\kappa = -A_3\left(\frac{2\pi}{L}\right)^2 = \frac{A_1}{7.56}\left(\frac{2\pi}{19}\right)^2 = A_1\ (.01446) \tag{B12}$$

so

$$\varepsilon_x = .01446\ A_1 z \qquad (B13)$$

The coordinate z varies in a piecewise linear manner with respect to the cross-sectional postion, s. The variation is given by

$$z = \frac{b_w}{2} = 0.625\ ; \qquad 0 \leq s \leq b_f$$

$$z = -\ s + \left(\frac{b_w}{2} + b_f\right) = 1.875 - s\ ; \qquad b_f \leq s \leq b_f + b_w \qquad (B14)$$

$$z = -\ \frac{b_w}{2} = -\ 0.625\ ; \qquad b_f + b_w \leq s \leq 2b_f + b_w$$

so substituting equations (B14) into (B13) gives

$$\varepsilon_x = .009038\ A_1\ ; \qquad 0 \leq s \leq b_f$$

$$\varepsilon_x = (.02711 - .01446\ s)\ A_1\ ; \qquad b_f \leq s \leq b_f + b_w \qquad (B15)$$

$$\varepsilon_x = -.009038\ A_1\ ; \qquad b_f + b_w \leq s \leq 2b_f + b_w$$

The cross-sectional strain distribution associated with torsional axis buckling is given in Brush and Almroth [15] as

$$\varepsilon_x = (\bar{\omega}_s - \omega_s)\ \phi'' \qquad (B16)$$

where ω_s is called the warping function and $\bar{\omega}_s$ is the cross-sectional average of the warping functionω_s. For this configuration, ω_s =1.674 in^2.

$$\phi'' = A_1\left(\frac{2\pi}{L}\right)^2 \cos\frac{2\pi x}{L} \qquad (B17)$$

At the midlength postion (x=L/2),

$$\phi'' = - A_1 \left(\frac{2\pi}{L}\right)^2 \tag{B18}$$

so

$$\varepsilon_x = - A_1 \left(\frac{2\pi}{L}\right)^2 (1.674 - \omega_s) = -.1094\ A_1\ (1.674 - \omega_s) \tag{B19}$$

The warping function ω_s , varies in a piecewise linear manner with respect to s. It is given by

$$\begin{aligned} \omega_s &= 0.625\ s\ ; && 0 \leq s \leq b_f \\ \omega_s &= 1.4509 - .5357\ s\ ; && b_f \leq s \leq b_f + b_w \\ \omega_s &= -1.4509 + 0.625\ s\ ; && b_f + b_w \leq s \leq 2b_f + b_w \end{aligned} \tag{B20}$$

so the strain distribution is given by

$$\begin{aligned} \varepsilon_x &= - A_1\ (.1831 - .06838\ s)\ ; && 0 \leq s \leq b_f \\ \varepsilon_x &= - A_1\ (.02441 + .05861\ s)\ ; && b_f \leq s \leq b_f\ b_w \\ \varepsilon_x &= - A_1\ (0.3419 - .06838\ s)\ ; && b_f + b_w \leq s \leq 2b_f + b_w \end{aligned} \tag{B21}$$

Adding the two strain distributions (B15) and (B21) gives

$$\varepsilon_x = - A_1 (.1741 - .06838\ s) ; \qquad 0 \leq s \leq b_f$$

$$\varepsilon_x = - A_1 (-.0027 + .07307\ s) ; \qquad b_f \leq s \leq b_f + b_w \tag{B22}$$

$$\varepsilon_x = - A_1 (.3509 - .06838\ s) ; \qquad b_f + b_w \leq s \leq 2b_f + b_w$$

Evaluating ε_x at s=0, b_f, b_f+b_w, and $2b_f+b_w$ gives

s	$\varepsilon_x/-A_1$
0	.1741
1.25	.0886
2.50	.1800
3.75	.0945

A plot of $\frac{\varepsilon_x}{-A_1}$ vs. cross-sectional postion, s, is shown in Figure 26. This distribution is due to torsional/strong-axis buckling only. The total strain distribution also includes a uniform compression distribution that shifts the entire distribution in a negative direction.

The vita has been removed from the scanned document